1   **Metamorphic chronology comes of age: past achievements and future prospects**

2   **Revision 1**

3

4   Matthew J. Kohn[1] (corresponding author)

5   [1]*Department of Geosciences, Boise State University, Boise, ID 83725;*

6   *mattkohn@boisestate.edu; phone: 208-426-2757; fax: 208-426-4061*

7

8   **Abstract**

9   Metamorphic chronology or petrochronology has steadily evolved over several decades

10   through ever improving analytical techniques and more complete understanding of the

11   geochemical and petrologic evolution of metamorphosing rocks. Here, the principal methods by

12   which we link metamorphic temperatures (T's) and ages (t's) are reviewed, focusing primarily on

13   accessory minerals. Methods discussed include textural correlation, inversion of diffusion

14   profiles, chemical correlation, and combined chronologic and thermometric microanalysis. Each

15   method demonstrates remarkable power in elucidating petrologic and tectonic processes, as

16   examples from several orogens illustrate, but limitations must also be acknowledged and help

17   define future research directions. Correlation methods are conceptually simple, but can be

18   relatively non-specific regarding pressure-temperature conditions of formation. A new

19   consideration of errors indicates that modeling of chronologic diffusion gradients provides

20   relatively precise constraints on cooling rates, whereas models of chemical diffusion gradients

21   can lead to large (factor of 2 or more) cooling rate uncertainties. Although arguably the best

22   method currently in use, simultaneous T-t measurements are currently limited zircon, titanite

23   and rutile. Directions for future improvement include investigation of diffusion profiles for

24   numerous trace element-mineral systems using now-routine depth profiling. New trace element

25   models will help improve chemical correlation methods. The determination of inclusion

26   entrapment P-T conditions based on Raman spectroscopic measurement of inclusion pressures

27   ("thermoba-Raman-try") may well revolutionize textural correlation methods.

28   **Keywords:** Geochronology: monazite, titanite, zircon; Trace elements and REE: Zr, zircon,

29   titanite, rutile; Metamorphic petrology: UHP

30

30   **Introduction**

31   Understanding Earth processes commonly depends on constraining rates. Although the

32   aphorism "*No dates, no rates*" is disproved by modeling chemical diffusion profiles (see below),

33   improvements in how we date minerals have indeed led to many major advances in

34   petrogenesis and tectonics. In the last couple decades, metamorphic geochronologists have

35   increasingly sought to develop new analytical and theoretical techniques to link ages with

36   temperature and/or mineral reactions and petrologic evolution. Referred to as

37   "petrochronology"[1] in some quarters, this integrative approach culminates a large body of

38   research in metamorphic geochronology, mineral chemistry, and petrogenesis. This review

39   considers four different ways in which we link metamorphic ages ("t") with temperature ("T"),

40   mainly in the context of accessory minerals: (1) Textural correlation between key minerals and

41   ages, (2) Inversion of diffusional zoning, both chemical zoning and chronologic zoning, (3)

42   Chemical correlation of ages to mineral growth events, and (4) Simultaneous microanalysis of

43   ages and trace-element temperatures in mineral domains. Examples, limitations, and

44   advantages are discussed. Last, some views are presented on research directions with good

45   future potential, including further development of geochemical tracers, new trace element

46   models, and the use of Raman spectroscopy for determining inclusion pressures and

47   temperatures ("thermoba-Raman-try", Kohn, 2014).

48

49   **Textural Correlation**

50   **Datable inclusions in a petrogenetically diagnostic host**

51   Many textural correlations rely on dating mineral inclusions inside a host mineral whose

52   chemistry or growth is somehow linked to P-T evolution. The most common host mineral is

53   garnet, both because it commonly grows with increasing P or T so its rim may represent the

54   peak of metamorphism, and because its chemistry can be inverted to constrain a P-T path.

---

[1] Engi (2009), but see also Fraser (1997) for the first use in the geosciences literature. Originally (Thompson, 1969), petrochronology was defined in reference to a Yoruba (west African) cult of the river god Eyinle, in which the number of stones in a ceremonial earthenware pot was proposed as a possible measure of duration and intensity of devotion, i.e. a sort of "stone-chronometer." As Thompson wrote (p. 141): "Future research will determine whether there is a mean correlation between years and stones. If there is, we have a [method] for the dating of the pots, a science that we take the liberty of designating in advance petrochronology."

2

55   Thus, the age for a garnet core vs. rim can inform rates of heating or loading, which can be

56   useful for tectonic interpretations and models of mineral growth kinetics. Conceptually, if an

57   accessory mineral continually reequilibrates during metamorphism, either via recrystallization or

58   diffusion, the measured age of inclusions at any point in a garnet gives the time of that stage of

59   growth. Alternatively, if accessory minerals do not completely reequilibrate (e.g., if they retain

60   relict cores), the youngest age at a radial position might be viewed as the best estimate of the

61   host phase age at that point. Both views assume that, once included, an accessory mineral is

62   inert to further reequilibration, both because it is isolated from the matrix, and because

63   diffusivities for many elements in garnet are slow. It is further assumed that some mechanism

64   drives continuous accessory mineral growth or recrystallization, a view that is rarely supported

65   theoretically.

66   Textural correlation is conceptually simple but results are not always easy to interpret.

67   Consider two rocks collected from near the Main Central Thrust (MCT) in the central Himalaya

68   investigated by Catlos et al. (2001). They used an ion microprobe to collect *in situ* ^{232}Th/^{208}Pb

69   ages in monazite grains from different textural settings. In one rock (Fig. 1A), monazite

70   inclusions in the rim of a garnet and matrix monazite grains show remarkably good age

71   correspondence: essentially all ages are between 6 and 7 Ma. These data were interpreted to

72   imply that monazite either reequilibrated during prograde metamorphism or grew near the

73   metamorphic peak, so the age of peak metamorphism, as reflected by final growth of the garnet

74   and matrix monazite grains, occurred about 6-7 Ma. This interpretation makes sense in a

75   regional context because monazite ages are systematically older in structurally higher rocks and

76   systematically younger in structurally lower rocks. But without identifying a specific monazite-

77   forming reaction from thermodynamic modeling (Spear and Pyle, 2010; Spear, 2010) or the

78   temperature of monazite formation from trace element thermometry (Pyle et al., 2001), the

79   likelihood that both garnet and monazite grew near the peak of metamorphism cannot be

80   assessed, and in fact for many bulk rock compositions monazite should dissolve as garnet

81   grows (Spear and Pyle, 2010). Thus, presuming the garnet rim grew near the peak of

82   metamorphism, the monazite age provides at most a maximum constraint (i.e. peak

83   metamorphism occurred ≤6-7 Ma). A minimum constraint must instead be derived from some

3

84   other source, for example muscovite ^{40}Ar/^{39}Ar cooling ages of 4-5 Ma from the same structural

85   level (Catlos et al., 2001). Overall, a relatively tight constraint on the peak of metamorphism is

86   possible in this area (6±1 Ma), but requires multiple chronologic systems.

87   A second rock from the next higher thrust sheet illustrates more serious age

88   complexities and ambiguities using textural correlation alone. Matrix grain ages range from 11 to

89   29 Ma, and an inclusion near the rim of the garnet is ≥30 Ma. These data were interpreted to

90   reflect early prograde metamorphism, with late stage resetting leading to the 11 Ma age. At the

91   time, the closure temperature of monazite to Pb loss was thought to be 600-650 °C (Smith and

92   Giletti, 1997), and the peak temperature of the rock was c. 750 °C, so 11 Ma was thought to

93   provide a minimum estimate of the age of peak metamorphism. Although Catlos et al.'s

94   interpretation of these ages may be correct, the ages say little about the timing of peak

95   metamorphism. Possibly it was ~11 Ma (the age of the youngest matrix monazite) or even

96   younger, or perhaps as old as ~30 Ma (the age of the youngest inclusion in garnet). For an

97   orogen whose lifetime spans <60 Ma, a 20 Ma range in ages leads to considerable ambiguity in

98   tectonic interpretations.

99   Usually we think that more data should lead to clearer interpretation, but this is not

100   always so. For example, Hoisch et al. (2008) dated numerous tiny monazite inclusions in

101   several garnets from the Grouse Creek Range, Utah, to provide a comprehensive dataset of

102   spatially distributed ages (Fig. 2). Ages generally decrease towards garnet rims, but with greater

103   scatter than expected from analytical error alone. Hoisch et al. (2008) interpreted the monazite

104   ages as decreasing linearly with increasing volume of garnet (Fig. 2A), which implicitly requires

105   that analytical errors are underestimated (by a factor of ~4). From a petrogenetic perspective,

106   without any information about the monazite-forming reaction(s), inclusion ages are only

107   maximum estimates of garnet growth ages, so do not directly constrain garnet growth rates.

108   Because garnet growth in many rocks is expected to drive monazite dissolution, not growth

109   (Spear and Pyle, 2010), the ages indicate only that garnet growth occurred later than ~40 Ma.

110   Even if one assumes that the youngest monazite age at any radial position does

111   accurately date the age of garnet at that point, a wholly different interpretation of garnet growth

112   rates is possible depending on how one views the data. Considering just one garnet (Fig. 2A),

4

113   the youngest monazite inclusion ages might be interpreted as nearly constant near the core,

114   gradually decreasing in the mid-region of the garnet, and nearly constant near the rim. This age

115   distribution implies that garnet grew rapidly (core), then slowly (mid-region), then rapidly again

116   (near-rim). In contrast, considering monazite inclusions from all garnets together (correlated

117   through garnet major element chemistry), a different garnet growth pattern is derivable – slow-

118   rapid-slow (Fig. 2B). These disparate views of garnet growth have little impact on tectonic

119   models for the region, but span the range of perspectives on how minerals grow – either slowly

120   and progressively (Hoisch et al., 2008) as temperature rises, or rapidly and abruptly (Fig. 2) as

121   nucleation or growth kinetics are overstepped, or garnet-forming reactions are crossed (e.g.

122   Walther and Wood, 1984; Ague and Baxter, 2007; see discussion of Pattison et al., 2011; Spear

123   et al., 2014). As this example illustrates, resolving the dynamics of mineral growth requires more

124   than just textural correlation.

125

126   **Petrogenetically diagnostic inclusions in a datable host**

127   A complementary approach to textural correlation relies on dating domains of a

128   chronologically useful host mineral that contains inclusions of a petrogenetically useful mineral.

129   Metamorphic zircons with diagnostic inclusions represent common targets for this type of

130   analysis. Investigation of ultra-high pressure (UHP) rocks from the Kaghan region, Pakistan

131   (Kaneko et al., 2003), exemplifies the power of this approach but also its limitations.

132   Cathodoluminescence images of zircons show distinct domains, with an inner detrital or protolith

133   core, a mantle that contains quartz inclusions, and a rim that contains coesite inclusions (Fig.

134   3A). Ion microprobe analyses of zircon from the quartz-bearing domains average ~50 Ma,

135   whereas analyses from the coesite-bearing domains average ~47 Ma (Fig. 3A). These ages are

136   absolutely crucial to interpreting Himalayan tectonics because they unequivocally indicate

137   subduction of the leading edge of the Indian plate to UHP conditions by 47 Ma. This age is quite

138   close to the interred age of initiation of continent-continent collision (c. 55 Ma; e.g. Najman et

139   al., 2010) and substantially predates peak metamorphism of the Himalayan metamorphic core

140   (c. 20 Ma; e.g. see summary of Godin et al., 2006).

141   But what exactly do the quartz-domain and coesite-domain ages mean in terms of

142   heating and burial rates? Without any other information, zircon could have grown around quartz

143   and coesite just as the rock crossed the quartz-coesite boundary, perhaps over a small

144   temperature range of only 10 °C. If so, heating and loading rates were extremely slow: 10°C/3

145   Ma ~ 3 °C/Ma (Fig. 3B). Alternatively, zircon could have grown around quartz at low T and

146   coesite at high T, say 450 and 700 °C respectively. If so, heating and loading rates were

147   extremely fast: 150°C/3 Ma = 50 °C/Ma (Fig. 3B). Although the importance of these ages on

148   Himalayan tectonics is truly profound, further exploration of petrogenesis and tectonics requires

149   additional quantitative information on the P-T conditions of inclusion entrapment, either through

150   identification of prograde zircon-forming reactions (although these are not predicted from mass

151   balance; Kohn et al., 2015), or through independent thermobarometry such as Ti-in-zircon

152   thermometry (Watson et al., 2006).

153

154   **Inclusion reequilibration?**

155   Not all inclusions or crystal interiors are inert to reequilibration. Dissolution-

156   reprecipitation has been proposed to explain garnet textures and chemical zoning in garnet

157   interiors in central Vermont (Hames and Menard, 1993), Norway (Pollok et al., 2008) and

158   Greece (Martin et al., 2011). Distinctive features include fluid inclusion clouds, chemically

159   defined embayments of garnet cores, chemically and texturally isolated "islands" (relict cores),

160   and cross-cutting chemical zones. Garnets from a rock in southern Chile show optical textures

161   (Fig. 4A) and chemical textures (Fig. 4B-D) comparable to other studies, including fluid inclusion

162   clouds, texturally and chemically isolated islands, and strong chemical zoning around inclusions

163   (low Ca, high Mn) irrespective of radial position. Even if dissolution-reprecipitation is not the

164   correct mechanism to explain these features, zoning in all major chemical components around

165   inclusions demonstrates that the radial position is not a good indicator of relative timing –

166   inclusions in the core and elsewhere are associated with garnet whose chemistry appears late.

167   Of significance to this discussion, chemical and textural reequilibration is evident around

168   seemingly isolated inclusions in the interior of the garnet. Sometimes healed fluid pathways

169   connect inclusions with the matrix (Fig. 4A), but other times such textures are not obvious (Fig.

170 4D). Other studies have argued for reequilibration of mineral inclusions, not just the host phase,

171 e.g. formation of coesite inside zircon cores (Gebauer et al., 1997) and recrystallization of

172 monazite inside garnets (Martin et al., 2007) but without obvious textural indicators like fluid

173 inclusions. Thus, a mineral inclusion and its host may not always be isolated from later

174 reequilibration, so textures alone do not always reliably link ages and petrogenesis.

175   Taken together, these studies caution that, although textural correlations can surely

176 provide invaluable chronologic information, interpretations should be tempered with the

177 realization that the ages provide limits only (not absolute P-T-t points), are not always very

178 sensitive to P-T conditions, and may be affected by later processes. While it is always valuable

179 to date mineral inclusions, or identify zones in datable minerals with distinct mineral inclusions,

180 complementary supporting evidence for any interpretation should be marshaled.

181

182   **Diffusion Zoning**

183 **Theory and errors.**

184   Diffusion zoning can be modeled to determine cooling rates in two different ways.

185 Classically, chemical zoning is modeled in terms of diffusional exchange between a slow-

186 diffusing host (usually garnet) and a fast diffusing reservoir (usually biotite; Lasaga, 1983).

187 Taking garnet-biotite as an example, if Fe-Mg exchange is the sole reaction affecting

188 compositions and volume diffusion within the garnet is the sole mechanism limiting that

189 exchange, the compositions of garnet and matrix biotite can be inverted to obtain a closure

190 temperature (T_c). The cooling rate (s, or "speed" of cooling) that is required to produce an

191 observed T_c at a particular radial position is then calculated numerically (Fig. 5A). Faster cooling

192 yields higher T_c's closer to the edge of the garnet, whereas slower cooling yields lower T_c's that

193 penetrate farther into the garnet interior. Calculations are simplest if the mode of biotite is large,

194 so it does not change composition, but other mode-dependent models are possible, albeit not

195 considered here. An analogous example involving accessory minerals involves inversion of Zr

196 zoning in rutile in the context of the Zr-in-rutile thermometer (Smye et al., 2014). Inversion of

197 chemical diffusion profiles is wholly independent of chronologic measurements, disproving the

198 view of many geochronologists that determining rates requires dates.

7

199   A complementary approach to the inversion of chemical zoning focuses on measuring

200   chronologic zoning, typically with depth profiling. In this case, diffusion models infer T_c for each

201   point, rather than s (Fig. 5B). Two different depths with different T_c's and ages provide an

202   estimate of s, derived by dividing the difference in calculated T_c's by their difference in age (i.e.

203    $s = \Delta T_c / \Delta t$).

204   Dodson (1986) derived a simple and elegant form of the position-dependent closure

205   temperature equation that applies to both types of calculations:

206
$$T_c(x) = \frac{E/R}{\ln\left[\dfrac{\varepsilon R T_c^2 D_o / a^2}{E \cdot s}\right] + 4S_2(x)}$$
(1)

207   where, T_c and $T_c(x)$ are the bulk and position-dependent closure temperatures, E and D_o are

208   activation energy and pre-exponential term in an Arrhenius-type diffusion expression, R is the

209   gas constant, a is the characteristic length scale of the mineral (e.g. radius of a spherical grain),

210   s is the cooling rate, ε is the exponential of Euler's constant, $4S_2(x)$ is a tabulated position-

211   dependent term, and x is the fractional distance from the mineral center. T_c and $T_c(x)$ are

212   insensitive to s (which appears in the logarithm of the denominator), so a large change in s is

213   required to balance a small change to T_c or $T_c(x)$.

214   To model chemical zoning, $T_c(x)$ at a particular position is determined *a priori* from

215   thermometry (e.g., garnet-biotite Fe-Mg exchange or Zr-in-rutile thermometry; Fig. 5A), and s is

216   adjusted for a specific pair of E and D_o values until the correct $T_c(x)$ is achieved. Uncertainties in

217   cooling rate can be calculated by propagating errors both in diffusion properties and calculated

218   T_c. For E and D_o, the value for E is perturbed by $+2\sigma$, the corresponding value for D_o is

219   calculated from experimental data (the two parameters are nearly perfectly correlated), and a

220   new cooling rate determined to produce the same $T_c(x)$. Calculations are then repeated for $E-2\sigma$

221   and its corresponding D_o. The difference in the cooling rates determined with the nominal values

222   of E and D_o vs. the perturbed values of E and D_o provides a measure of the propagated

223   uncertainty in s (Fig. 5C). The propagated analytical error in $T_c(x)$ (c. ± 5 °C for garnet-biotite:

224   Kohn and Spear, 1991b; as low as ± 2 °C for Zr-in rutile) is typically smaller than propagated

225   errors in E and D_o and is ignored here.

8

226   To model chronologic zoning, the ages at two positions are determined *a priori*, a "seed"

227   value for s is assumed, and $T_c(x)$ values for diffusional reequilibration of the radiogenic daughter

228   element are calculated using Equation 1 (Fig. 5B). An apparent cooling rate, s*, is calculated

229   from pairs of $T_c(x)$ and age (from the relation s* = $\Delta T_c/\Delta t$) and substituted for s in Equation 1

230   iteratively until s*=s. Again, values for E and D_o may be varied within $\pm 2\sigma$ uncertainty, resulting

231   in new $T_c(x)$ values and cooling rates (Fig. 5C). Chronologic error should also be propagated,

232   specific to the isotopic and analytical system that is investigated, but is not considered here

233   because it is quite sample-specific and error propagation is straightforward.

234   Uncertainties in diffusion properties propagate to considerably different uncertainties in

235   cooling rates if chemical vs. chronologic zoning is modeled. As an example, uncertainties in

236   diffusion parameters for Mg diffusion in garnet (Carlson, 2006) were propagated numerically for

237   a 1 mm radius grain cooling at 25 °C/Ma. Inversion of chemical zoning using Equation 1 yields a

238   range of possible cooling rates between 15 and 45 °C/Ma, i.e. about a factor of 2 (Fig. 5C).

239   Garnet is one of the best-studied minerals, so errors for other minerals are likely to be larger

240   than calculated here. To make a direct comparison with chronologic zoning models, the same

241   diffusion coefficients and their uncertainties were propagated assuming they pertained to a

242   radiogenic system. This results in a ~7% error in cooling rate, i.e. a nominal rate of 25°C/Ma

243   could range between 23 and 27 °C (Fig. 5C). Thus, inversion of chronologic zoning rather than

244   chemical zoning is inherently more precise, as long as chronologic errors are not too large.

245   Calculated cooling rates tend to converge towards true cooling rates close to the

246   physical edge of a mineral (Fig. 5C). But these calculations then become quite susceptible to

247   slight growth or consumption, which moves the grain edge and changes the assumed length

248   scale. For example, at 5 μm from the crystal edge, uncertainties in diffusion rates propagate to

249   only ~30% error in calculated s when inverting chemical compositions (i.e. between 18 and 35

250   °C/Ma; Fig. 5C). Shifting the grain boundary inward by 5 μm, however, so that the present 5μm

251   position was originally 10 μm from the edge, increases calculated s by a factor of 4 (up to 100

252   °C/Ma). Dissolution shortens profiles and (erroneously) implies faster cooling rates, whereas

253   growth lengthens profiles and (erroneously) implies slower cooling rates. Similar calculations for

9

254   chronologic zoning suggest bias by a factor of ~2 – still smaller than inversion of chemical

255   zoning, but substantially larger than for a fixed boundary.

256   A final complication for inverting chemical profiles concerns how one models boundary

257   compositions. For garnet, most models assume that its rim composition is controlled solely by

258   retrograde exchange reactions (ReER's; e.g., Fe-garnet + Mg-biotite = Mg-garnet + Fe-biotite).

259   Garnet compositions at high temperatures, however, are more likely controlled by retrograde

260   net-transfer reactions (ReNTR's), which involve the net consumption or production of a mineral

261   (e.g., garnet + K-feldspar + melt = sillimanite + biotite + plagioclase + quartz). Thermodynamic

262   models demonstrate that garnet rim compositions are far more sensitive to temperature during

263   operation of ReNTR's than ReER's (Spear, 2004). So, even if the physical position of the garnet

264   rim remains fixed, cooling rates that are calculated assuming that compositions are controlled

265   by ReER's vs. ReNTR's can differ by 1-2 orders of magnitude (Spear, 2004). Understanding the

266   reaction history of the rock is clearly key for accurate modeling.

267

268   **Examples.**

269   Garnets from a Himalayan gneiss in Sikkim, India, provide an example of chemically-

270   based geospeedometry (Ganguly et al., 2000; Fig. 6). Two different garnets show comparable

271   zoning in Mg# towards their rims (Fig. 6A). Overall, this zoning is consistent with an average

272   cooling rate of ~20 °C/Ma. In combination with a 1-D thermal model, Ganguly et al. (2000)

273   inferred accelerated cooling from 15 °C/Ma at 800 °C to ~200 °C/Ma at 450 °C. Chemical

274   zoning in all 4 major components on the rims of garnets (Fig. 6B), however, suggest that the

275   physical edge of the garnet might not have remained fixed and/or that rim compositions were

276   affected by a ReNTR, not just Fe-Mg exchange. Slight resorption of the garnet rim, as

277   suggested by a rimward increase in Mn, would lead to overestimated late-stage cooling rates,

278   whereas operation of a ReNTR at high T, such as melt crystallization, would lead to

279   underestimated initial cooling rates. Thus, although a transition from slow cooling in the deep

280   crust to rapid cooling in the shallow crust is completely consistent with petrologic observations,

281   especially the formation of high-T, low-P assemblages (Ganguly et al., 2000), quantifying

282   cooling rates using chemical zoning may have large uncertainties.

10

283   Chronologically-based geospeedometry was first attempted by using an ion microprobe
284   to depth profile monazite from a Himalayan pegmatite in central Nepal (Grove and Harrison,
285   1999). A decreasing age profile over the outer ~1.5 μm of the crystal was modeled in terms of
286   diffusive loss to infer rapidly decreasing cooling rates. Later experimental data on Pb diffusion in
287   monazite (Cherniak et al., 2004; Gardés et al., 2007), however, imply that diffusive resetting is
288   unlikely over even 0.1 μm distances. The decreasing age profile may instead reflect slight
289   growth of monazite during cooling, which could be tested by analyzing other elements such as
290   Y, Th, REE, etc. that respond to reactions. Analogously, although titanite U-Pb ages have
291   traditionally been viewed as susceptible to diffusive resetting (Cherniak, 1993), depth profiles
292   from high-grade titanite from the central Himalaya indicate that Pb diffuses too slowly at T≤800
293   °C to reset ages over micron length scales (Kohn and Corrie, 2011). Recent U-Pb data from
294   rutile (Smye and Stockli, 2014) are the best current candidate of diffusive chronologic closure
295   profiles in accessory minerals. A steadily decreasing age towards rutile rims, especially over the
296   outer ~10 μm, is consistent with moderately rapid cooling between 185 and 175 Ma, followed by
297   slower cooling to ~150 Ma.

298

299   **Chemical Correlation**

300   Chemical correlation attempts to link chemistry with the rock's reaction history using
301   geochemical and petrologic principles. In its simplest conceptual form, mineral compositions
302   and the mass distributions of elements evolve during metamorphism, so by measuring the
303   composition of whatever mineral (domain) is dated, an age can be linked to overall petrologic
304   evolution, constraining the P-T condition of formation.

305

306   **Monazite**

307   Monazite is well studied, and research spans at least 15 years (e.g., Pyle and Spear,
308   1999, 2003; Pyle et al., 2001; Kohn et al., 2004, 2005; Kelly et al., 2006; Rubatto et al., 2013).
309   In general, Th and Y contents of monazite decrease during solid-state metamorphic reactions,
310   leading to Rayleigh-like depletions from core to rim (Fig. 8). For Y, decreases are linked to
311   growth of garnet, which also depletes the rock in available Y (Fig. 8). Our understanding of

11

312 mineralogical distributions of Th is quite limited, so Th contents cannot be so simply linked to

313 other minerals (except possibly allanite; Spear, 2010). Regardless, Th contents in monazite are

314 so high, any growth is likely to deplete the matrix and any later-grown monazite in Th.

315 Interpretations beyond this level are restricted by relatively poor understanding of how other

316 trace elements behave during metamorphism. For example, Corrie and Kohn (2008) were

317 unable to mass balance many REE and concluded that grain boundary adsorption of REE might

318 be important. Thus, even grain coarsening in the absence of prograde reactions might affect

319 REE budgets and the growth and chemistry of monazite.

320   Partial melting changes compositional systematics dramatically because monazite is

321 soluble in partial melts (Rapp et al., 1987; Montel, 1993). The most important reaction for

322 metasediments is the muscovite dehydration-melting reaction, which occurs at T~700 °C in

323 typical bulk compositions (Spear et al., 1999). Upon melt crystallization, new monazite grows,

324 commonly as high-Y and -Th overgrowths on relict prograde grains (Pyle and Spear, 2003;

325 Kohn et al., 2004). These chemical principles allow identification of early-formed monazite (older

326 high-Y and high-Th domains not on rims), monazite that formed in a late-prograde solid-state

327 assemblage (low-Y and -Th domains; ≤ ~700 °C), and post-anatectic monazite (high-Y and -Th

328 overgrowths; ≤700 °C). Peak metamorphic monazite in anatectic rocks is generally not expected

329 because monazite should be dissolving.

330   Use of monazite chemistry for refining age interpretations is now widespread, and the

331 following example from the Himalaya (Kohn et al., 2004, 2005) illustrates its power in the

332 context of previous textural-only interpretations. In the Modi and Langtang areas of central

333 Nepal, Kohn et al. (2004, 2005) and Corrie and Kohn (2011) studied several different structural

334 levels (Fig. 9A) and identified several different compositionally and texturally distinct populations

335 of monazite in each level (Fig. 9B): early prograde (high-Y and high-Th), late prograde (low-Y

336 and low-Th), post-anatectic (high-Y and high-Th rims), and alteration (low-Y along cross-cutting

337 fractures). A pre-Himalayan, high-U grain was also found. In anatectic rocks, late-prograde and

338 post-anatectic compositions bracket the timing of melting and peak metamorphism, whereas in

339 lower-grade rocks, late-prograde compositions limit the timing of peak metamorphism (Fig. 9B).

340 Knowing peak metamorphic temperatures from thermobarometry (Kohn, 2008) and the

12

341   temperature of the muscovite dehydration-melting reaction, these data can be placed into a

342   petrologically consistent thermal and tectonic model of orogenic wedge development (Fig. 9C).

343   For example, crystallization of post-anatectic monazite from the highest structural level sampled

344   along the Langtang transect at ~18 Ma occurred while the next structural level (the MCT sheet)

345   was still heating to its peak (at c. 16 Ma – between late-prograde and post-anatectic monazite

346   ages). These data suggest thrust emplacement between 16 and 18 Ma, simultaneously cooling

347   the upper plate and warming the lower plate. The same chronologic patterns continue down-

348   section: the MCT sheet was cooling and crystallizing its melts at ~16 Ma while the next lower

349   thrust sheet was still heating (early prograde monazite ages). This lower sheet had cooled

350   through muscovite closure to Ar by at least 7.5 Ma, prior to peak metamorphism of the

351   structurally lowest sheet. These patterns are expected for in-sequence growth of an orogenic

352   wedge, but this example is the first clear documentation of this process in the Himalaya, and

353   perhaps anywhere on Earth. Just as in the study of Catlos et al. (2001), a single rock or thrust

354   sheet could exhibit a large range of monazite ages (e.g., 16 to 36 Ma in the MCT sheet at

355   Langtang). Combination of ages with chemistry, however, links monazite ages with the rock's

356   reaction history and broad regions of P-T space, which permits refined tectonic interpretations

357   compared to textural-only interpretations.

358   The main complication in using monazite chemical correlation lies in its lack of

359   compositional specificity. Although the temperature-time condition of melt crystallization can be

360   determined with some confidence, the precise temperature of other dated domains can often be

361   assigned only more generally. For example, in subsolidus rocks at Langtang the lowest-Y

362   monazite domains were assigned to the peak of metamorphism, whereas they could have

363   formed earlier. This ambiguity does not change the main tectonic interpretations in Nepal, but

364   might elsewhere. And although a Y-in-monazite thermometer has been calibrated (Pyle et al.,

365   2001), it requires compositional correlation with several minerals. The ultimate correlation

366   method would provide a direct measure of temperature or pressure from the dated domain itself,

367   but no such method has yet been proposed for monazite.

368

369   **Zircon**

13

370   Chemical correlation methods have been proposed for zircon, particularly in reference to

371   REE patterns (Rubatto, 2002; Whitehouse and Platt, 2003; Fig. 10). Fundamentally,

372   interpretations focus on two features: the presence or absence of a Eu-anomaly, and the

373   flatness of MREE-HREE patterns. Both methods emphasize mass balance. Europium warrants

374   particular attention because, although the concepts appear founded in simple mass balance and

375   petrologic principles, closer scrutiny suggests unresolved complications.

376   In most rocks, plagioclase takes up unusually high concentrations of Eu relative to other

377   REE, so when plagioclase is stable, it should contain a disproportionate fraction of Eu, and all

378   other minerals should have a negative Eu anomaly. As rocks transition to the eclogite facies,

379   plagioclase breaks down to produce omphacite and garnet, which do not take up unusual

380   amounts of Eu relative to other REE. Thus, plagioclase breakdown releases Eu back to the

381   rock, flooding the rock with its reserve of Eu. Zircon formed in the plagioclase-stable field might

382   be expected to have more pronounced negative Eu anomalies than zircon formed in the eclogite

383   facies (Rubatto, 2002).

384   While this mass balance argument appears plausible, it overlooks valence state – Eu

385   taken up by plagioclase is divalent, whereas Eu taken up by zircon (and most other minerals) is

386   trivalent. Therefore, breakdown of plagioclase and liberation of Eu^{2+} may have no impact on

387   uptake of Eu^{3+} in zircon and consequently its Eu anomaly. One solution to this conundrum is to

388   hypothesize that initial growth of metamorphic plagioclase nuclei takes up all available Eu^{2+}, and

389   redox reactions cause partial conversion of residual Eu^{3+} to Eu^{2+}. Progressive growth of

390   plagioclase and sequestration of Eu^{2+} ultimately removes virtually all Eu from the rock (similar to

391   Mn uptake in garnet), and this Eu is now nearly all divalent. When plagioclase breaks down to

392   form omphacite, a substantial amount of this Eu^{2+} is converted back to Eu^{3+} to maintain redox

393   equilibrium, removing the Eu anomaly in zircon and other minerals. If this hypothesis is correct,

394   however, any process that allows plagioclase to equilibrate with the whole-rock will allow its

395   Eu^{2+} to replenish the Eu^{3+} reservoir and contribute to REE patterns in other minerals. For

396   example, deformation-driven recrystallization or simple heating could enable Eu in plagioclase

397   interiors to rejoin the reactive rock. The diffusion rate of Eu^{2+} in plagioclase is not known, but

398   data for Sr suggest that diffusive equilibration may be possible at temperatures at or below ~600

14

399   °C (Cherniak and Watson, 1992, 1994). Therefore, the demise of a Eu anomaly in zircon, even

400   if it is related to plagioclase equilibration, may not reflect a transition to the eclogite facies, but

401   rather crossing a threshold temperature or strain rate.

402   Overall, MREE and HREE patterns in zircon are interpreted in the context of garnet

403   growth. Prior to garnet formation, zircon REE patterns are assumed to have steep positive

404   slopes (Rubatto, 2002). Although the composition of a detrital zircon could be wholly unrelated

405   to the host rock, depending on sediment sources, compilations of sediment and igneous

406   compositions show relatively flat overall REE patterns (as normalized to chondrites; Fig. 10A).

407   Because zircon strongly favors HREE to LREE compared to whole rocks (Sano et al., 2002),

408   zircon compositions for average (meta-) sediments or mantle-sourced igneous rocks are

409   predicted to exhibit steep REE patterns (Fig. 10A). Thus, it is not surprising that many detrital

410   (usually igneous) zircon cores have steep REE patterns. Such a pattern is also generally

411   predicted for metamorphic zircons that form in either metasedimentary or metaigneous rocks, as

412   long as no other major sink of MREE and HREE is present (Fig. 10A). Why, then, do many

413   metamorphic zircon overgrowths exhibit flat MREE-HREE patterns (Fig. 10B)? This chemical

414   trend is consistent with growth of garnet because it preferentially takes up HREE. That is, garnet

415   growth depletes the reactive matrix in HREE and causes HREE-depletion (flatter MREE-HREE

416   patterns; Rubatto, 2002; Whitehouse and Platt, 2003), both in zircon (Fig. 10A) and

417   progressively in garnet (Fig. 10B).

418   The main question that this discussion raises is: what constraints do flat MREE-HREE

419   patterns place on the P-T conditions of zircon formation? Theoretically, not much. Garnet is

420   stable over an enormous region of P-T space (Fig. 10C), and a zircon could in principle form

421   anytime from days to billions of years after garnet nucleation. Consequently, the conditions of

422   zircon formation may not be significantly restricted. In fact, considering that metamorphic

423   petrologists commonly study rocks that still contain (metastable) garnet crystals, a hypothetical

424   zircon formed today, long after any metamorphic event and well outside the garnet stability field,

425   would also be predicted to show a flat MREE-HREE pattern. Identifying that zircon formed in the

426   presence of garnet surely does support the view that a zircon age is syn- to post-metamorphic,

427   and such an age for a rock or terrane can be tectonically useful. But clearer delineation of the P-

15

428   T conditions of zircon formation and placement of the age in a coherent petrologic context

429   requires additional, more detailed, petrology and thermobarometry.

430

431   **Direct Combined Thermometry and Geochronology**

432   The latest research seeks to link ages directly with temperature through simultaneous

433   geochronology and trace element thermometry in single microanalytical spots. Zircon, titanite

434   and rutile are all amenable to geochronologic and thermometric microanalysis, exploiting the U-

435   Pb system and the experimentally calibrated Ti-in-zircon, Zr-in-titanite, and Zr-in-rutile

436   thermometers (Watson et al., 2006; Tomkins et al., 2007; Hayden et al., 2008). Applications

437   depend on relative diffusivities of Pb vs. thermometric trace elements. Diffusion of Pb and Ti in

438   zircon is extremely slow (Cherniak and Watson, 2001, 2007), so zircon domains should faithfully

439   preserve both their Ti-in-zircon temperatures and U-Pb ages over virtually all metamorphic

440   conditions. Titanite's Zr diffusivity is sufficiently slow that it should retain its Zr temperature up to

441   at least 750 °C (Cherniak, 2006) and Himalayan titanite data (Kohn and Corrie, 2011) show no

442   evidence of near-rim (≤ 2 μm) diffusive reequilibration of Zr at peak temperatures of 775 °C.

443   Although experiments suggest relatively fast Pb diffusivities in titanite, with a typical T_c of c. 600

444   °C (Cherniak, 1993), recent chronologic data can be explained only if Pb diffusion is extremely

445   slow, with a T_c of at least ~800 °C. For example, depth profiling of titanite crystal faces from c.

446   775 °C rocks in the Himalaya cannot be reconciled with models of diffusive Pb loss (Kohn and

447   Corrie, 2011), and titanite cores in rocks from the Western Gneiss Region retain protolith ages

448   of c. 1 Ga despite Caledonian UHP metamorphism that culminated in temperatures of ~780 °C

449   (Spencer et al., 2013). If Pb diffusivities were as fast as indicated experimentally, diffusion

450   profiles should be ubiquitous in such high-T grains, and older ages should be eradicated. Thus,

451   although experimentally and empirically-determined diffusivities for other elements and minerals

452   are commonly compatible, experimental results for Pb diffusion in titanite appear exceptionally

453   incompatible with nature. Rutile has faster diffusivities for Pb and Zr with typical T_c's of 600-650

454   °C (Cherniak, 2000; Vry and Baker, 2006; Cherniak et al., 2007). Thus, rutile inclusions might

455   be used to constrain prograde temperature-time points, whereas matrix grains in higher-T rocks

456   could be modeled in terms of diffusive loss (Smye and Stockli, 2014).

457

Titanite

459   Investigation of calc-silicate titanite crystals in the Himalaya (Kohn and Corrie, 2011; Fig.

460   11A) illustrates how thermometry and chronology can be combined to improve understanding of

461   a rock's thermal history. Samples from the anatectic Greater Himalayan Sequence in the Modi

462   region of central Nepal reached peak temperatures of c. 775 °C (Corrie and Kohn, 2011). Both

463   depth profiling and spot analysis of grains in thin section showed significant differences in

464   temperature (Zr content) and U-Pb age that were inconsistent with diffusive resetting. By

465   measuring both temperature and age for each spot, these data suggest slow heating from ~700

466   °C to ~780 °C between ~35 and ~25 Ma, followed by slight cooling to ~765 °C by ~21 Ma (Fig.

467   11A). Rapid cooling commenced immediately afterwards, as indicated regionally by monazite

468   crystallization from *in situ* anatectic melts at 20±2 Ma and muscovite $^{40}Ar/^{39}Ar$ ages of 14-15 Ma

469   (Godin et al., 2001). If diffusion did not bias these observations, they require much more

470   protracted heating than commonly considered for the Himalaya. This result is important for

471   crustal geodynamics because it implies that hot weak zones can exist in the crust for millions of

472   years without nucleating or focusing shear structures (Kohn and Corrie, 2011).

473   A complementary study of titanite from the Western Gneiss Region (Spencer et al.,

474   2013) suggests that regional temperature-time histories can be inferred through microanalysis

475   of this mineral in multiple rocks (Fig. 11B). Spencer et al. (2013) combined numerous trace

476   element and U-Pb microanalyses of different titanite grains from individual rocks to infer each

477   rock's average temperature and age. This approach assumes data for a sample represent a

478   single population of grains, which is true for most albeit not all of their rocks. Although less

479   elegant than a crystal-domain-specific approach, combining data improves chronologic

480   resolution, which can be necessary in older orogens where individual spot analyses carry large

481   age uncertainty. For example, in the Himalaya a 5-10% error may be tolerable (only ±1-3 Ma)

482   whereas in the Paleozoic, the same relative error translates to much larger absolute

483   uncertainties (±20-40 Ma), which can impede tectonic interpretations. Some datapoints for

484   Western Gneiss Region titanites are obvious outliers and inspection of raw data indicates they

485   do not conform to a single population, but exhibit a bimodal distribution of Zr contents or ages;

17

486   these are ignored in the present discussion. Overall, the titanite dataset suggests high T as

487   early as 405 Ma, followed by rapid cooling to muscovite closure by 380-385 Ma (Young et al.,

488   2011; Fig. 11B). Titanite is unstable above P~15 kbar in these rocks (Spencer et al., 2013;

489   inset, Fig. 11B), so, unlike in the Himalayan calc-silicates, titanite illuminates the late stage

490   exhumation and thermal history, not early-stage processes. Models for petrologic evolution of

491   UHP rocks in western Norway imply that temperatures must have been similarly high near

492   maximum pressures, implying a flat earlier temperature-time history (dashed line, Fig. 11B).

493   Until Spencer et al.'s work, views on the age of high-pressure (HP) and UHP metamorphism

494   had ranged from ~395 to ~425 Ma (e.g. see summary of Kylander-Clark et al., 2009). Because

495   titanite is a late-stage, relatively low-P mineral, however, the titanite data demand HP and UHP

496   metamorphism before ~405 Ma.

497

498   **Zircon**

499   Because of slow intracrystalline diffusivities, zircon is an obvious target for combined

500   thermometry and geochronology, but relatively little systematic work has yet attempted to

501   construct temperature-time histories or compare with other independent data. Zircons from

502   Himalayan leucogranites and migmatites in the Sikkim region of India (between Nepal and

503   Bhutan) are worth considering because recent studies provide a rich dataset (Kellett et al.,

504   2013; Rubatto et al., 2013), and because such data potentially elucidate interactions among

505   melt formation, thrust movement, and lower crustal flow. The following discussion is somewhat

506   complex, but illustrates the limits of interpretability of zircon metamorphic chronology.

507   Several factors in the context of host-rock T-t paths impact expected temperatures

508   recorded by these anatectic magmas and their zircons. (1) Inherited zircons are common, so the

509   melts were always saturated in zircon. This permits additional application of whole-rock zircon-

510   saturation thermometry (Watson and Harrison, 1983; Boehnke et al., 2013) as a cross-check to

511   Ti-in-zircon temperatures. However, zircon inheritance implies that calculated zircon-saturation

512   temperatures are maxima. (2) Both *in situ* and cross-cutting melts are thought to have formed

513   via muscovite dehydration-melting (Inger and Harris, 1992; Harris and Massey, 1994), which

514   occurs at c. 700 °C in plagioclase-bearing rocks (Spear et al., 1999; dry solidus, Fig. 12A).

18

515   Without other consideration, this implies that most Ti-in-zircon and zircon-saturation

516   temperatures should be at least 700 °C. (3) A low-temperature zircon cannot crystallize in a

517   high-temperature host-rock, so the host-rock T-t path limits the region of T-t space available to

518   Ti-in-zircon temperatures (Permissible vs. Forbidden Zones, Fig. 12A). For example, for the

519   hypothetical T-t curve in Fig. 12A, a 700 °C zircon could crystallize only ≥34 or ≤13 Ma, not near

520   the peak of metamorphism. (4) If host-rock temperatures increase after muscovite dehydration-

521   melting, any melts present in the host-rock should continue to dissolve zircon and consequently

522   record zircon saturation temperatures greater than or equal to the peak temperature. Magmas

523   formed after the peak of metamorphism might record lower temperatures. (5) Himalayan

524   leucogranites are famous for high boron contents (Searle and Fryer, 1986), which lowers the

525   solidus by 50-100 °C (Chorlton and Martin, 1978). Fractional crystallization or concentration of

526   H_2O into melts might also lead to solidus temperatures closer to the wet solidus. If so, magmatic

527   zircons might crystallize at even lower temperatures, perhaps as low as 550 °C, but again only

528   very early or very late in the metamorphic evolution (schematically ≥35 or ≤10 Ma, Fig. 12A).

529   Two main chronologic datasets have been collected from leucogranites and migmatites

530   in the Sikkim region (Kellett et al., 2013; Rubatto et al., 2013). Petrologic studies there

531   consistently infer high host-rock temperatures that persisted during quasi-isothermal

532   exhumation from ~10 to ~4 kbar (Neogi et al., 1998; Ganguly et al., 2000; Harris et al., 2004;

533   Rubatto et al., 2013). Fit to thermal models, these paths imply temperature-time histories that

534   peak at ~800 °C and cool rapidly thereafter (Fig. 12B). Different studies infer different paths (in

535   part depending on structural level; green lines, Fig. 12B), but all broadly show rapid cooling

536   around 15-20 Ma and high temperatures at 20-25 Ma. The timing of peak metamorphic

537   conditions is based on changes to monazite chemistry in dated grains (Rubatto et al., 2013),

538   dated peritectic garnets (Harris et al., 2004), and geochronology of high-grade rocks in the

539   region (e.g., Li et al., 2003; Cottle et al., 2009b; Corrie et al., 2010). Thus, we expect that Ti-in-

540   zircon temperatures should fall above specific proposed T-t curves, with an absence of low-T

541   ages between ~15 and ~25 Ma.

542   Nearly all zircon data strikingly contradict expectations, as nearly all fall below proposed

543   T-t histories for host-rocks, and are well below 800 °C between 15 and 25 Ma. The low Ti-in-

19

544   zircon temperatures, however, are completely consistent with zircon-saturation temperatures

545   inferred from a synthesis of Himalayan leucogranites (Kohn, 2013; Fig. 12B). Thus the data

546   create a major interpretational conflict. The zircon data are internally consistent – Ti-in-zircon

547   and zircon-saturation temperatures are consistently low, and make sense in the context of low

548   solidus temperatures expected for boron-rich melts. However, these data imply that

549   temperatures must have been less than 600-650 °C since 25-30 Ma, whereas petrologic and

550   alternate geochronologic data indicate otherwise. Apparently one (or more) of three

551   observations must be discounted: the petrologic interpretations of high temperatures, the timing

552   of peak metamorphism, or the combined Ti-in-zircon and zircon-saturation temperatures.

553   Several studies now argue that the same structural levels elsewhere in the Himalaya

554   attained temperatures commensurate with partial melting by c. 35 Ma (Kohn and Corrie, 2011;

555   Imayama et al., 2012; Thöni et al., 2012; Rubatto et al., 2013; Wang et al., 2013). Although

556   many ages >25 Ma likely reflect subsolidus prograde metamorphism (Kohn et al., 2004, 2005;

557   Cottle et al., 2009a; Langille et al., 2012; Stübner et al., 2014), possibly the high temperature

558   assemblages at Sikkim were produced prior to ~30 Ma, disconnecting peak metamorphism from

559   zircon and leucogranite crystallization. That is, the "Forbidden Zone" (Fig. 12A) might predate

560   the zircon ages (Fig. 12B). Alternatively, high-T (low-P) assemblages at Sikkim might reflect

561   local heating associated with intrusions, so that although local temperatures were high (briefly),

562   regional temperatures were low, causing sequential crystallization of melts. The

563   correspondence between Ti-in-zircon and zircon-saturation temperatures argues against

564   thermometer inaccuracies. Further research integrating petrology with geochronology will be

565   needed to resolve this issue.

566

567   **Discussion**

568   **Pros and Cons**

569   Clearly, methods of linking chronologic and petrologic data have evolved substantially

570   over the last 20 years. This trend is illustrated by my own microanalytical research, which

571   progressed from texturally-based studies (Catlos et al., 2001; Kohn et al., 2001), to

572   petrologically and chronologically linked research (Kohn et al., 2004, 2005; Corrie and Kohn,

20

573   2011), to direct chronologic and thermometric analysis (Kohn and Corrie, 2011). Each approach

574   brings advantages and disadvantages, and every method will work well in some rocks.

575   Inclusions, if unaltered after entrapment, surely imply that the host mineral crystallized during or

576   after formation of the inclusion mineral, so the age of the inclusion either dates or predates that

577   zone in the host mineral. This simple concept has substantial power, for example in the

578   identification of early UHP metamorphism in the Himalaya (Kaneko et al., 2003; Fig. 3).

579   Nonetheless, a little geochemistry can improve interpretations substantially. The composition of

580   monazite, particularly Y and Th contents, distinguishes different generation domains and allows

581   refined tectonic interpretations (Kohn, 2008; Fig. 9). Although simultaneous chronology and

582   thermometry has particular power, this approach is not feasible for many minerals or rocks. For

583   example, monazite is chronologically invaluable, but has no simple trace element thermometer

584   (the Pyle et al., 2001, Y-in-monazite thermometer requires compositional correlation with

585   several other minerals), so studies must continue to emphasize chemistry in the context of

586   models. In contrast, rutile's low U content makes chronology difficult, but high Zr makes

587   thermometry comparatively easy. The lingering discrepancies in the Himalaya between

588   petrologic temperatures and regional geochronology vs. Ti-in-zircon and zircon-saturation

589   temperatures are particularly worrying. Overall, data that combine geochronology and

590   thermometry are as yet too sparse to pronounce judgment, but the potential payoffs are

591   substantial, and further exploration of the systematics in different minerals is needed.

592

593   **New Directions and Implications**

594   Future work can and should expand the use of geochemically-based (petrochronologic)

595   methods. For example, relatively routine depth-profiling methods for trace elements open a vast

596   array of potential mineral-element systems amenable to the inversion of chemical diffusion

597   profiles to infer cooling rates. Further exploration of this method might tax the patience of

598   experimentalists, as petrologists request data on an ever-increasing list of elements and

599   minerals. Ultimately, however, this work will refine our understanding of diffusion rates and

600   element mobility during metamorphism, and steadily reduce cooling rate uncertainties. Similarly,

601   new measurements of ever-larger arrays of trace elements in chronologically useful minerals

602   like monazite will help identify P-T conditions of formation more precisely. Besides these rather

603   obvious directions, two other potential realms of inquiry are considered – modeling and

604   thermoba-Raman-try. The former is a necessary complement to geochemical methods now in

605   practice. The latter represents an entirely new direction of research and promises a new era in

606   textural correlation studies by quantifying pressures and temperatures of inclusion entrapment.

607

608   **Modeling.** Trace element abundances and distributions among metamorphic minerals

609   fundamentally control accessory mineral stability and growth. In contrast to numerous models

610   for common rock-forming silicates and oxides, fewer models address accessory minerals. A few

611   studies have tackled monazite (Janots et al., 2007; Kelsey et al., 2008; Spear, 2010; Spear and

612   Pyle, 2010), emphasizing Y and REE, but the difficulties of accounting for individual trace

613   elements to model REE patterns are substantial and quantitative attempts are as yet lacking. At

614   least one empirical study has implicated grain boundaries as a reservoir for REE (Corrie and

615   Kohn, 2008), which further complicates modeling. Zircon is more amenable to theoretical

616   modeling because, to a first order, Zr is the only trace element that requires mass balancing.

617   Models have now been constructed for metapelites (Kelsey et al., 2008; Kelsey and Powell,

618   2011; Kohn et al., 2015) and metabasites (Kohn et al., 2015), and results provide broad

619   recommendations for interpreting zircon ages. Models from Kohn et al. (2015) are discussed

620   here because they consider Zr partitioning among metamorphic minerals more comprehensively

621   and extend to higher pressures relevant to UHP terranes (35, rather than 12 kbar in Kelsey et

622   al., 2008, and Kelsey and Powell, 2011).

623   In Kohn et al.'s models, modes and Zr contents of minerals were monitored along three

624   representative P-T paths (Fig. 13). For metabasite models (Fig. 13A, B), two different

625   thermochemical databases were used (Berman, 1988 and Berman and Aranovich, 1996;

626   Holland and Powell, 1998). For metapelites (Fig. 13C, D), the Holland and Powell (1998)

627   thermochemical database was used. Each model shows essentially the same basic pattern –

628   the matrix takes up increasing amounts of Zr during prograde metamorphism, particularly rutile

629   in metabasites and melts in metapelites. Thus the mode of zircon decreases until the maximum

630   temperature (in metabasites) or maximum melt content (in metapelites) is reached (Fig. 13A-D;

22

631   see also Kelsey and Powell, 2011). Depending on the P-T path, the reduction in zircon mode

632   can be moderate (c. 10%) to large (c. 50%). During exhumation and cooling, Zr is returned to

633   the matrix to form new zircon, especially as melts crystallize and low-Zr ilmenite or titanite

634   replaces high-Zr rutile. These results suggest that metamorphic zircon should mainly record the

635   later stages of metamorphism, not peak or prograde processes. Obviously zircon might actually

636   grow on the prograde path because of other processes that are not included in models, such as

637   dissolution of metamict or micro-grains elsewhere in a rock with reprecipitation onto relict grains

638   (Dempster et al., 2008). For example, the older quartz-bearing domains in the Kaneko et al.

639   (2003) study might represent such a case. In general, such processes simply redistribute

640   existing zircon, however, and most metamorphic zircon is predicted to form relatively late.

641   Zircon ages from the Western Gneiss Region of Norway (Fig. 13E) generally conform to

642   model predictions. Titanite ages provide unequivocal evidence for the timing of late-stage

643   exhumation and cooling, certainly below ~15 kbar (Spencer et al., 2013; Figs. 11B, 13C).

644   Metamorphic zircon ages (Carswell et al., 2003b; Root et al., 2004; Young et al., 2007; Krogh et al.,

645   2011; Gordon et al., 2013; Beckman et al., 2014) show that the ages of most (~70%) zircons

646   overlap titanite ages (Fig. 13E). Like titanite, zircon must have formed at relatively low-P late in

647   the region's metamorphic evolution. These results are consistent with Sm-Nd garnet ages,

648   which also overlap zircon ages (Fig. 13E). Diffusivities of Nd in garnet are sufficiently fast that

649   ages in these rocks should dominantly reflect closure at temperatures of 700-800 °C (Burton et

650   al., 1995; Ganguly et al., 1998), depending on grain size and cooling rate, and rarely reflect

651   maximum pressures. Some zircon ages overlap Lu-Hf garnet ages (Kylander-Clark et al., 2009)

652   and a Th-Pb age of a monazite inclusion in garnet (Terry et al., 2000; Fig. 13E). These might

653   reflect either prograde metamorphism or maximum pressures, but only a minority of zircon ages

654   falls within this range. Overall, these data reinforce the conclusion that metamorphic zircon

655   should commonly be a late-crystallizing phase.

656   The general success of modeling zircon notwithstanding, inclusions of prograde

657   metamorphic minerals in zircons demonstrate that mass balance and element partitioning

658   cannot solely control mineral growth. Future work must identify what other factors control

659   formation of accessory minerals. For minerals like monazite, apatite and allanite, a much better

660   understanding of REE, Th, P and F is needed. Models will require substantial prior effort to

661   constrain partitioning among metamorphic minerals and identify reservoirs of trace elements, as

662   well as constrain the kinetics of trace element movement in metamorphic rocks. Numerous

663   reports of compositional oscillations, sector zoning, and patchy zoning for trace elements in

664   garnet (e.g., Spear and Kohn, 1996; Chernoff and Carlson, 1999; Yang and Rivers, 2001, 2002;

665   Lapen et al., 2003; Kohn, 2004, 2013; Vielzeuf et al., 2005) suggest that kinetics plays a major

666   role and that development of fully quantitative models will prove challenging.

667

668   **Thermoba-Raman-try.** Although Raman spectroscopy on mineral inclusions has been

669   applied for about 15 years to recover pressures of original entrapment (Izraeli et al., 1999;

670   Sobolev et al., 2000), concurrent and subsequent theoretical developments (Zhang, 1998;

671   Guiraud and Powell, 2006; Kohn, 2014; Kouketsu et al., 2014) and applications to common

672   crustal rocks (Enami et al., 2007; Ashley et al., 2014; Spear et al., 2014) have recently

673   promoted this technique to the leading edge of thermobarometric research. At the time of

674   inclusion entrapment, no differential pressure occurs between inclusion and host mineral.

675   Because host and inclusion have different thermal expansivities and compressibilities, however,

676   a differential pressure develops during exhumation and cooling. As originally developed by

677   Rosenfeld and Chase (1961) the line of permissible entrapment conditions of an inclusion can

678   be calculated (subject to certain geometric constraints) based on the present-day magnitude of

679   the pressure on the inclusion, the volume equation of state of the host and inclusion, and the

680   shear modulus of the host. Many host-inclusion pairs are quite pressure-sensitive (e.g. quartz-

681   in-garnet, "QuiG"), whereas others are decidedly temperature-sensitive (e.g. zircon-in-garnet,

682   "ZiG"; Fig. 14A).

683   Raman confocal microspectroscopy plays a key role by measuring band position shifts

684   of *in situ* inclusions relative to standard state spectra. Raman band positions depend on

685   pressure, and that dependence has been calibrated for numerous common minerals. Thus,

686   Raman band shifts for inclusions can be inverted to infer present-day inclusion pressures, and

687   the present-day pressures can be inverted using standard calibrations to identify entrapment

688   conditions (e.g. Kohn, 2014; Fig. 14A, B). This combination of the use of Raman spectroscopy

24

689 in thermobarometric endeavors gives rise to the term "thermoba-Raman-try" (Kohn, 2014). The

690 analytical uncertainties on retrieved P-T conditions are encouragingly small: only a few hundred

691 bars for quartz inclusions in numerous minerals (garnet, clinopyroxene, epidote, ilmenite,

692 kyanite, lawsonite, magnetite, staurolite, titanite, tourmaline, rutile and zircon), and a few tens of

693 degrees for zircon in several minerals (garnet, clinopyroxene, epidote, kyanite, and titanite;

694 Kohn, 2014; Fig. 14A, B). Because analysis is wholly non-destructive, even these acceptably

695 small errors can be reduced through multiple repeat analyses of the same inclusion.

696   An example from the Himalaya illustrates the correspondence that is possible between

697 thermoba-Raman-try and conventional thermobarometry. Corrie and Kohn (2011) conducted a

698 regional study of metamorphic rocks in the Modi region of central Nepal. One rock from the

699 Greater Himalayan Sequence crystallized at an inferred peak P-T condition of ~750 °C and 11-

700 12 kbar (Fig. 14A). Quartz and zircon inclusions occur near the edge of garnets from this rock,

701 and thermoba-Raman-try on them intersects at a P-T condition of about 11 kbar and 725 °C,

702 close to, albeit slightly lower than the conventional thermobarometric estimate. The difference is

703 within analytical error, but the Raman-based estimate could also reflect either a P-T condition

704 prior to the metamorphic peak or slight reequilibration during exhumation and cooling.

705   Further exploration of thermoba-Raman-try is needed to identify its practical strengths

706 and weaknesses, but published examples already predict a new era for P-T studies. Although

707 inference of entrapment pressures using coesite inclusions is doomed for most rocks because

708 of partial transition to quartz (Guiraud and Powell, 2006; Kohn, 2014; see also Ye et al., 2001;

709 Korsakov et al., 2010), the quartz-in-zircon, quartz-in-titanite and quartz-in-rutile barometers

710 appear promising (Fig. 14B). These specific barometers are potentially quite useful. For

711 example, zircon ages from quartz-bearing domains analyzed by Kaneko et al. (2000; Fig. 3)

712 could in principle be coupled with Ti-in-zircon temperatures and quartz-in-zircon pressures to

713 determine specific P-T-t points. Such observations would define better both the prograde P-T

714 path and rates of subduction and heating. Similarly quartz inclusions in Himalayan titanite could

715 be used to identify rates of burial or exhumation during protracted heating. In contrast, Zr-

716 modeling and regional geochronology suggest that quartz inclusions in zircons from the

717 Scandinavian Caledonides would help constrain retrograde P-T conditions and exhumation

25

718   rates. In this context, the greatest power of thermoba-Raman-try may lie in identifying

719   pressures, rather than temperatures, of inclusion entrapment. In many petrologic and tectonic

720   interpretations, metamorphic depths and how they change through time prove more useful than

721   temperature. Possibly thermoba-Raman-try will help fill this gap in our petrochronologic toolbox.

722

723

723 **Acknowledgments**

724 Thanks are due Jesse Walters for measuring Raman spectra on quartz and zircon inclusions in

725 the Himalayan garnet, to Frank Spear and an anonymous reviewer for helpful comments, and to

726 Frank Spear for collecting X-ray maps on the Chilean garnet. Funded by NSF grants

727 EAR1048124 and EAR1321897.

728

728   **References cited**

729   Ague, J.J., and Baxter, E.F. (2007) Brief thermal pulses during mountain building recorded by Sr

730   diffusion in apatite and multicomponent diffusion in garnet. Earth and Planetary Science

731   Letters, 261, 500-516.

732   Arevalo, R.J., and McDonough, W.F. (2010) Chemical variations and regional diversity

733   observed in MORB. Chemical Geology, 271, 70-85.

734   Ashley, K.T., Caddick, M.J., Steele-MacInnis, M.J., Bodnar, R.J., and Dragovic, B. (2014)

735   Geothermobarometric history of subduction recorded by quartz inclusions in garnet.

736   Geochemistry, Geophysics, Geosystems, 15, 350-360.

737   Beckman, V., Möller, C., Söderlund, U., Corfu, F., Pallon, J., and Chamberlain, K.R. (2014)

738   Metamorphic zircon formation at the transition from gabbro to eclogite in Trollheimen-

739   Surnadalen, Norwegian Caledonides. Geological Society, London, Special Publications,

740   390, 403-424.

741   Berman, R.G. (1988) Internally-consistent thermodynamic data for minerals in the system Na_2O-

742   K_2O-CaO-MgO-FeO-Fe_2O_3-Al_2O_3- SiO_2-TiO_2-H_2O-CO_2. Journal of Petrology, 29, 445-522.

743   Berman, R.G., and Aranovich, L.Y. (1996) Optimized standard state and solution properties of

744   minerals 1. Model calibration for olivine, orthopyroxene, cordierite, garnet, and ilmenite in

745   the system FeO-MgO-CaO-Al_2O_3-TiO_2-SiO_2. Contributions to Mineralogy and Petrology,

746   126, 1-24.

747   Boehnke, P., Watson, E.B., Trail, D., Harrison, T.M., and Schmitt, A.K. (2013) Zircon saturation

748   re-revisited. Chemical Geology, 351, 324-334.

749   Burton, K.W., Kohn, M.J., Cohen, A.S., and O'Nions, R.K. (1995) The relative diffusion of Pb,

750   Nd, Sr and O in garnet. Earth and Planetary Science Letters, 133, 199-211.

751   Carlson, W.D. (2006) Rates of Fe, Mg, Mn, and Ca diffusion in garnet. American Mineralogist,

752   91, 1-11.

753   Carosi, R., Montomoli, C., Rubatto, D., and Visona, D. (2013) Leucogranite intruding the South

754   Tibetan Detachment in western Nepal: implications for exhumation models in the Himalayas.

755   Terra Nova, 25, 478-489.

28

756   Carswell, D.A., Tucker, R.D., O'Brien, P.J., and Krogh, T.E. (2003b) Coesite micro-inclusions

757   and the U/Pb age of zircons from the Hareidland Eclogite in the Western Gneiss Region of

758   Norway. Lithos, 67, 181-190.

759   Catlos, E.J., Harrison, T.M., Kohn, M.J., Grove, M., Ryerson, F.J., Manning, C.E., and Upreti,

760   B.N. (2001) Geochronologic and thermobarometric constraints on the evolution of the Main

761   Central Thrust, central Nepal Himalaya. Journal of Geophysical Research-Solid Earth,

762   106(B8), 16177-16204.

763   Cherniak, D.J. (1993) Lead diffusion in titanite and preliminary results on the effects of radiation

764   damage on Pb transport. Chemical Geology, 110, p. 177-194.

765   Cherniak, D.J. (2000) Pb diffusion in rutile. Contributions to Mineralogy and Petrology, 139(2),

766   198-207.

767   Cherniak, D.J. (2006) Zr diffusion in titanite. Contributions to Mineralogy and Petrology, 152,

768   639-647.

769   Cherniak, D.J., and Watson, E.B. (1992) A study of strontium diffusion in K-feldspar, Na-K

770   feldspar and anorthite using Rutherford backscattering spectroscopy. Earth and Planetary

771   Science Letters, 113(3), 411-425.

772   Cherniak, D.J., and Watson, E.B. (1994) A study of strontium diffusion in plagioclase using

773   Rutherford backscattering spectroscopy. Geochimica et Cosmochimica Acta, 58(23), 5179-

774   5190.

775   Cherniak, D.J., and Watson, E.B. (2001) Pb diffusion in zircon. Chemical Geology, 172(1-2), 5-

776   24.

777   Cherniak, D.J., and Watson, E.B. (2007) Ti diffusion in zircon. Chemical Geology, 242, 470-483.

778   Cherniak, D.J., Watson, E.B., Grove, M., and Harrison, T.M. (2004) Pb diffusion in monazite: a

779   combined RBS/SIMS study. Geochimica et Cosmochimica Acta, 68, 207-226.

780   Cherniak, D.J., Manchester, J., and Watson, E.B. (2007) Zr and Hf diffusion in rutile. Earth and

781   Planetary Science Letters, 261, 267-279.

782   Chernoff, C.B., and Carlson, W.D. (1999) Trace element zoning as a record of chemical

783   disequilibrium during garnet growth. Geology, 27(6), 555-558.

784   Chorlton, L.B., and Martin, R.F. (1978) The effect of boron on the granite solidus. Canadian

785   Mineralogist, 16, 239-244.

786   Corrie, S.L., and Kohn, M.J. (2008) Trace-element distributions in silicates during prograde

787   metamorphic reactions: implications for monazite formation. Journal of Metamorphic

788   Geology, 26(4), 451-464.

789   Corrie, S.L., and Kohn, M.J. (2011) Metamorphic history of the central Himalaya, Annapurna

790   region, Nepal, and implications for tectonic models. Geological Society of America Bulletin,

791   123(9-10), 1863-1879.

792   Corrie, S.L., Kohn, M.J., and Vervoort, J.D. (2010) Young eclogite from the Greater Himalayan

793   Sequence, Arun Valley, eastern Nepal: P-T-t path and tectonic implications. Earth and

794   Planetary Science Letters, 289(3-4), 406-416.

795   Cottle, J.M., Searle, M.P., Horstwood, M.S.A., and Waters, D.J. (2009a) Timing of midcrustal

796   metamorphism, melting, and deformation in the Mount Everest region of southern Tibet

797   revealed by U(-Th)-Pb geochronology. Journal of Geology, 117(6), 643-664.

798   Cottle, J.M., Jessup, M.J., Newell, D.L., Horstwood, M.S.A., Noble, S.R., Parrish, R.R., Waters,

799   D.J., and Searle, M.P. (2009b) Geochronology of granulitized eclogite from the Ama Drime

800   Massif: Implications for the tectonic evolution of the South Tibetan Himalaya. Tectonics, 28,

801   TC1002.

802   Dempster, T.J., Hay, D.C., Gordon, S.H., and Kelly, N.M. (2008) Micro-zircon: origin and

803   evolution during metamorphism. Journal of Metamorphic Geology, 26, 499-507.

804   Dodson, M.H. (1986) Closure profiles in cooling systems. Materials Science Forum, 7, 145-154.

805   Enami, M., Nishtyama, T., and Mouri, T. (2007) Laser Raman microspectrometry of

806   metamorphic quartz: A simple method for comparison of metamorphic pressures. American

807   Mineralogist, 92(8-9), 1303-1315.

808   Engi, M. (2009) Petrochronology in the Central Alps: Results, implications, gaps. Mineralogical

809   Society of Great Britain and Ireland Abstracts with Program, annual meeting.

810   Fraser, G., Ellis, D., and Eggins, S. (1997) Zirconium abundance in granulite-facies minerals,

811   with implications for zircon geochronology in high-grade rocks. Geology, 25, 607-610.

812   Ganguly, J., Tirone, M., and Hervig, R.L. (1998) Diffusion kinetics of samarium and neodymium

813   in garnet, and a method for determining cooling rates of rocks. Science, 281, 805-807.

814   Ganguly, J., Dasgupta, S., Cheng, W., and Neogi, S. (2000) Exhumation history of a section of

815   the Sikkim Himalayas, India: records in the metamorphic mineral equilibria and

816   compositional zoning of garnet. Earth and Planetary Science Letters, 183, 471-486.

817   Gardés, E., Montel, J.-M., Seydoux-Guillaume, A.-M., and Wirth, R. (2007) Pb diffusion in

818   monazite: New constraints from the experimental study of Pb2+ <=> Ca2+ interdiffusion.

819   Geochimica et Cosmochimica Acta, 71, 4036-4043.

820   Gebauer, D., Schertl, H.P., Brix, M., and Schreyer, W. (1997) 35 Ma old ultrahigh-pressure

821   metamorphism and evidence for very rapid exhumation in the Dora Maira Massif, Western

822   Alps. Lithos, 41, 5-24.

823   Godin, L., Grujic, D., Law, R.D., and Searle, M.P. (2006) Channel flow, ductile extrusion and

824   exhumation in continental collision zones: an introduction. Geological Society Special

825   Publication, 268, 1-23.

826   Gordon, S.M., Whitney, D.L., Teyssier, C., and Fossen, H. (2013) U-Pb dates and trace-element

827   geochemistry of zircon from migmatite, Western Gneiss Region, Norway: Significance for

828   history of partial melting in continental subduction. Lithos, 170-171, 35-53.

829   Gromet, L.P., Dymek, R.F., Haskin, L.A., and Korotev, R.L. (1984) The "North American shale

830   composite"; its compilation, major and trace element characteristics. Geochimica et

831   Cosmochimica Acta, 48, 2469-2482.

832   Grove, M., and Harrison, T.M. (1999) Monazite Th-Pb age depth profiling. Geology, 27(6), 487-

833   490.

834   Guiraud, M., and Powell, R. (2006) P-V-T relationships and mineral equilibria in inclusions in

835   minerals. Earth and Planetary Science Letters, 244(3-4), 683-694.

836   Guo, Z., and Wilson, M. (2012) The Himalayan leucogranites: Constraints on the nature of their

837   crustal source region and geodynamic setting. Gondwana Research, 22, 360-376.

838   Hames, W.E., and Menard, T. (1993) Fluid-assisted modification of garnet composition along

839   rims, cracks, and mineral inclusion boundaries in samples of amphibolite facies schists.

840   American Mineralogist, 78(3-4), 338-344.

841   Harris, N., and Massey, J. (1994) Decompression and anatexis of Himalayan metapelites.

842   Tectonics, 13(6), 1537-1546.

843   Harris, N.B.W., Caddick, M., Kosler, J., Goswami, S., Vance, D., and Tindle, A.G. (2004) The

844   pressure-temperature-time path of migmatites from the Sikkim Himalaya. Journal of

845   Metamorphic Geology, 22(3), 249-264.

846   Hayden, L.A., Watson, E.B., and Wark, D.A. (2008) A thermobarometer for sphene (titanite).

847   Contributions to Mineralogy and Petrology, 155, 529-540.

848   Herman, F., Copeland, P., Avouac, J.-P., Bollinger, L., Mahéo, G., Le Fort, P., Rai, S., Foster,

849   D., Pecher, A., Stüwe, K., and Henry, P. (2010) Exhumation, crustal deformation, and

850   thermal structure of the Nepal Himalaya derived from inversion of thermochronological and

851   thermobarometric data and modeling of the topography. Journal of Geophysical Research,

852   115, doi:10.1029/2008/JB006126.

853   Hoisch, T.D., Wells, M.L., and Grove, M. (2008) Age trends in garnet-hosted monazite

854   inclusions from upper amphibolite-facies schist in the northern Grouse Creek Mountains,

855   Utah. Geochimica et Cosmochimica Acta, 72, 5505-5520.

856   Holland, T.J.B., and Powell, R. (1998) An internally consistent thermodynamic data set for

857   phases of petrological interest. Journal of Metamorphic Geology, 16(3), 309-343.

858   Imayama, T., Takeshita, T., Keewook, Y., Cho, D.-L., Kitajima, K., Tsutsumi, Y., Kayama, M.,

859   Nishido, H., Okumura, T., Yagi, K., Itaya, T., and Sano, Y. (2012) Two-stage partial melting

860   and contrasting cooling history within the Higher Himalayan Crystalline Sequence in the far-

861   eastern Nepal Himalaya. Lithos, 134-135, 1-22.

862   Inger, S., and Harris, N.B.W. (1992) Tectonothermal evolution of the High Himalayan crystalline

863   sequence, Langtang Valley, northern Nepal. Journal of Metamorphic Geology, 10(3), 439-

864   452.

865   Izraeli, E.S., Harris, J.W., and Navon, O. (1999) Raman barometry of diamond formation. Earth

866   and Planetary Science Letters, 173(3), 351-360.

867   Janots, E., Brunet, F., Goffé, B., Poinssot, C., Burchard, M., and Cemič, L. (2007)

868   Thermochemistry of monazite-(La) and dissakisite-(La): implications for monazite and

869   allanite stability in metapelites. Contributions to Mineralogy and Petrology, 154, 1-14.

870   Kaneko, Y., Katayama, I., Yamamoto, H., Misawa, K., Ishikawa, M., Rehman, H.U., Kausar,
871   A.B., and Shiraishi, K. (2003) Timing of Himalayan ultrahigh-pressure metamorphism:
872   sinking rate and subduction angle of the Indian continental crust beneath Asia. Journal of
873   Metamorphic Geology, 21(6), 589-599.

874   Kellett, D.A., Grujic, D., Coutand, I., Cottle, J., and Mukul, M. (2013) The South Tibetan
875   detachment system facilitates ultra rapid cooling of granulite-facies rocks in Sikkim
876   Himalaya. Tectonics, 32, doi:10.1002/tect.20014.

877   Kelly, N.M., Clarke, G.L., and Harley, S.L. (2006) Monazite behaviour and age significance in
878   poly-metamorphic high-grade terrains: A case study from the western Musgrave Block,
879   central Australia. Lithos, 88, 100-134.

880   Kelsey, D.E., and Powell, R. (2011) Progress in linking accessory mineral growth and
881   breakdown to major mineral evolution in metamorphic rocks: a thermodynamic approach in
882   the Na_2O-CaO-K_2O-FeO-MgO-Al_2O_3-SiO_2-H_2O-TiO_2-ZrO_2 system. Journal of Metamorphic
883   Geology, 29, 151-166.

884   Kelsey, D.E., Clark, C., and Hand, M. (2008) Thermobarometric modelling of zircon and
885   monazite growth in melt-bearing systems: examples using model metapelitic and
886   metapsammitic granulites. Journal of Metamorphic Geology, 26, 199-212.

887   Ketcham, R.A. (2005) Forward and inverse modeling of low-temperature thermochronometry
888   data. Reviews in Mineralogy and Geochemistry, 58, 275-314.

889   Kohn, M.J. (2004) Oscillatory- and sector-zoned garnets record cyclic (?) rapid thrusting in
890   central Nepal. Geochemistry Geophysics Geosystems, 5, 10.1029/2004gc000737.

891   Kohn, M.J. (2008) P-T-t data from central Nepal support critical taper and repudiate large-scale
892   channel flow of the Greater Himalayan Sequence. Geological Society of America Bulletin,
893   120(3-4), 259-273.

894   Kohn, M.J. (2013) Geochemical zoning in metamorphic minerals. In R. Rudnick, Ed. Treatise on
895   Geochemistry, volume 3, The Crust, p. 229-261. Elsevier.

896   Kohn, M.J. (2014) "Thermoba-Raman-try": Calibration of spectroscopic barometers and
897   thermometers for mineral inclusions. Earth and Planetary Science Letters, 388, 187-196.

33

898   Kohn, M.J., and Corrie, S.L. (2011) Preserved Zr-temperatures and U-Pb ages in high-grade
899   metamorphic titanite: evidence for a static hot channel in the Himalayan orogen. Earth and
900   Planetary Science Letters, 311, 136-143.

901   Kohn, M.J., and Malloy, M.A. (2004) Formation of monazite via prograde metamorphic reactions
902   among common silicates: Implications for age determinations. Geochimica et Cosmochimica
903   Acta, 68(1), 101-113.

904   Kohn, M.J., and Spear, F.S. (1991a) Error propagation for barometers: 1. Accuracy and
905   precision of experimentally located end-member reactions. American Mineralogist, 76, 128-
906   137.

907   Kohn, M.J., and Spear, F.S. (1991b) Error propagation for barometers: 2. Application to rocks.
908   American Mineralogist, 76, 138-147.

909   Kohn, M.J., Catlos, E.J., Ryerson, F.J., and Harrison, T.M. (2001) Pressure-temperature-time
910   path discontinuity in the Main Central thrust zone, central Nepal. Geology, 29(7), 571-574.

911   Kohn, M.J., Wieland, M.S., Parkinson, C.D., and Upreti, B.N. (2004) Miocene faulting at plate
912   tectonic velocity in the Himalaya of central Nepal. Earth and Planetary Science Letters,
913   228(3-4), 299-310.

914   Kohn, M.J., Wieland, M.S., Parkinson, C.D., and Upreti, B.N. (2005) Five generations of
915   monazite in Langtang gneisses: implications for chronology of the Himalayan metamorphic
916   core. Journal of Metamorphic Geology, 23(5), 399-406.

917   Kohn, M.J., Corrie, S.L., and Markley, C. (2015) The fall and rise of metamorphic zircon.
918   American Mineralogist, in press.

919   Korsakov, A.V., Zhukov, V.P., and Vandenabeele, P. (2010) Raman-based geobarometry of
920   ultrahigh-pressure metamorphic rocks: applications, problems, and perspectives. Analytical
921   and Bioanalytical Chemistry, 397(7), 2739-2752.

922   Kouketsu, Y., Nishiyama, T., Ikeda, T., and Enami, M. (2014) Evaluation of residual pressure in
923   an inclusion-host system using negative frequency shift of quartz Raman spectra. American
924   Mineralogist, 99, 433-442.

925   Krogh, T.E., Kamo, S.L., Robinson, P., Terry, M.P., and Kwok, K. (2011) U-Pb zircon
926   geochronology of eclogites from the Scandian Orogen, northern Western Gneiss Region,

927   Norway: 14-20 million years between eclogite crystallization and return to amphibolite-facies

928   conditions. Canadian Journal of Earth Science, 48, 441-472.

929   Kylander-Clark, A.R.C., Hacker, B.R., Johnson, C.M., Beard, B.L., and Mahlen, N.J. (2009)

930   Slow subduction of a thick ultrahigh-pressure terrane. Tectonics, 28,

931   doi:10.1029/2007TC002251.

932   Langille, J.M., Jessup, M.J., Cottle, J.M., Lederer, G., and Ahmad, T. (2012) Timing of

933   metamorphism, melting and exhumation of the Leo Pargil dome, northwest India. Journal of

934   Metamorphic Geology, 30(8), 769-791.

935   Lapen, T.J., Johnson, C.M., Baumgartner, L.P., Mahlen, N.J., Beard, B.L., and Amato, J.M.

936   (2003) Burial rates during prograde metamorphism of an ultra-high-pressure terrane: an

937   example from Lago di Cignana, western Alps, Italy. Earth and Planetary Science Letters,

938   215, 57-72.

939   Lasaga, A.C. (1983) Geospeedometry: An extension of geothermometry. In S.K. Saxena, Ed.

940   Kinetics and Equilibrium in Mineral Reactions, p. 81-114. Springer-Verlag, New York.

941   Li, D.W., Liao, Q.N., Yuan, Y.M., Wan, Y.S., Liu, D.M., Zhang, X.H., Yi, S.H., Cao, S.Z., and

942   Xie, D.F. (2003) SHRIMP U-Pb zircon geochronology of granulites at Rimana (Southern

943   Tibet) in the central segment of Himalayan Orogen. Chinese Science Bulletin, 48(23), 2647-

944   2650.

945   Liu, Z.-C., Wu, F.Y., Ji, W.Q., Wang, J.-G., and Liu, C.-Z. (2014) Petrogenesis of the Ramba

946   leucogranite in the Tethyan Himalaya and constraints on the channel flow model. Lithos,

947   208-209, 118-136.

948   Martin, A.J., Gehrels, G.E., and DeCelles, P.G. (2007) The tectonic significance of (U,Th)/Pb

949   ages of monazite inclusions in garnet from the Himalaya of central Nepal. Chemical

950   Geology, 244(1-2), 1-24.

951   Martin, L.A.J., Ballevre, M., Boulvais, P., Halfpenny, A., Vanderhaeghe, O., Duchene, S., and

952   E., D. (2011) Garnet re-equilibration by coupled dissolution-reprecipitation: evidence from

953   textural, major element and oxygen isotope zoning of 'cloudy' garnet. Journal of

954   Metamorphic Geology, 29, 213-231.

955   Montel, J.-M. (1993) A model for monazite/melt equilibrium and application to the generation of

956   granitic magmas. Chemical Geology, 110, 127-146.

957   Najman, Y., Appel, E., Boudagher-Fadel, M., Bown, P., Carter, A., Garzanti, E., Godin, L., Han,

958   J., Liebke, U., Oliver, G., Parrish, R., and Vezzoli, G. (2010) Timing of India-Asia collision:

959   Geological, biostratigraphic, and palaeomagnetic constraints. Journal of Geophysical

960   Research, 115, doi:10.1029/2010JB007673.

961   Neogi, S., Dasgupta, S., and Fukuoka, M. (1998) High P-T polymetamorphism, dehydration

962   melting, and generation of migmatites and granites in the Higher Himalayan Crystalline

963   Complex, Sikkim, India. Journal of Petrology, 39(1), 61-99.

964   Pattison, D.R.M., De Capitani, C., and Gaidies, F. (2011) Petrological consequences of

965   variations in metamorphic reaction affinity. Journal of Metamorphic Geology, 29, 953-977.

966   Pollok, K., Lloyd, G.E., Austrheim, H., and Putnis, A. (2008) Complex replacement patterns in

967   garnets from Bergen Arcs eclogites: a combined EBSD and analytical TEM study. Chemie

968   der Erde, 68, 177-191.

969   Putnis, A. (2002) Mineral replacement reactions: from macroscopic observations to microscopic

970   mechanisms. Mineralogical Magazine, 66, 689-708.

971   Pyle, J.M., and Spear, F.S. (1999) Yttrium zoning in garnet: coupling of major and accessory

972   phases during metamorphic reactions. Geological Materials Research, 1, 1-49.

973   Pyle, J.M., and Spear, F.S. (2003) Four generations of accessory-phase growth in low-pressure

974   migmatites from SW New Hampshire. American Mineralogist, 88, 338-351.

975   Pyle, J.M., Spear, F.S., Rudnick, R.L., and McDonough, W.F. (2001) Monazite-xenotime-garnet

976   equilibrium in metapelites and a new monazite-garnet thermometer. Journal of Petrology,

977   42, 2083-2107.

978   Rapp, R.P., Ryerson, F.J., and Miller, C.F. (1987) Experimental evidence bearing on the

979   stability of monazite during crustal anatexis. Geophysical Research Letters, 14, 307-310.

980   Root, D.B., Hacker, B.R., Mattinson, J.M., and Wooden, J.L. (2004) Zircon geochronology and

981   ca. 400 Ma exhumation of Norwegian ultrahigh-pressure rocks: an ion microprobe and

982   chemical abrasion study. Earth and Planetary Science Letters, 228, 325-341.

36

983   Rosenfeld, J.L., and Chase, A.B. (1961) Pressure and temperature of crystallization from elastic

984   effects around solid inclusions in minerals? American Journal of Science, 259, 519-541.

985   Rubatto, D. (2002) Zircon trace element geochemistry: partitioning with garnet and link between

986   U-Pb ages and metamorphism. Chemical Geology, 184, 123-138.

987   Rubatto, D., Chakraborty, S., and Dasgupta, S. (2013) Timescales of crustal melting in the

988   Higher Himalayan Crystallines (Sikkim, Eastern Himalaya) inferred from trace element-

989   constrained monazite and zircon chronology. Contributions to Mineralogy and Petrology,

990   165(2), 349-372.

991   Sano, Y., Terada, K., and Fukuoka, T. (2002) High mass resolution ion microprobe analysis of

992   rare earth elements in silicate glass, apatite, and zircon: lack of matrix dependency.

993   Chemical Geology, 184, 217-230.

994   Scaillet, B., France-Lanord, C., and Le Fort, P. (1990) Badrinath-Gangotri plutons (Garhwal,

995   India): petrological and geochemical evidence for fractionation processes in a high

996   Himalayan leucogranite. Journal of Volcanology and Geothermal Research, 44, 163-188.

997   Searle, M.P., and Fryer, B.J. (1986) Garnet, tourmaline and muscovite-bearing leucogranites,

998   gneisses and migmatites of the Higher Himalayas from Zanskar, Kulu, Lahoul and Kashmir.

999   In M.P. Coward, and A.C. Ries, Eds. Collision Tectonics, 19, p. 185-201. Geological Society

1000   Special Publication, London.

1001   Skora, S., Baumgartner, L.P., Mahlen, N.J., Johnson, C.M., Pilet, S., and Hellebrand, E. (2006)

1002   Diffusion-limited REE uptake by eclogite garnets and its consequences for Lu-Hf and Sm-Nd

1003   geochronology. Contributions to Mineralogy and Petrology, 152, 703-720.

1004   Smith, H.A., and Giletti, B.J. (1997) Lead diffusion in monazite. Geochimica et Cosmochimica

1005   Acta, 61(5), 1047-1055.

1006   Smye, A.J., and Stockli, D.F., 2014. Rutile U-Pb age depth profiling: a continuous record of

1007   lithospheric thermal evolution. Earth and Planetary Science Letters, 408, 171-182.

1008   Smye, A.J., Stöckli, D.F., and Zack, T. (2014) Tracing lithospheric thermal evolution with high

1009   field strength element speedometry in rutile. EOS - Transactions of the American

1010   Geophysical Union, V54B-08

37

1011 Sobolev, N.V., Fursenko, B.A., Goryainov, S.V., Shu, J.F., Hemley, R.J., Mao, H.K., and Boyd,

1012   F.R. (2000) Fossilized high pressure from the Earth's deep interior: The coesite-in-diamond

1013   barometer. Proceedings of the National Academy of Sciences, 97(22), 11875-11879.

1014 Spear, F.S. (2004) Fast cooling and exhumation of the Valhalla metamorphic core complex,

1015   southeastern British Columbia. International Geology Review, 46, 193-209.

1016 Spear, F.S. (2010) Monazite-allanite phase relations in metapelites. Chemical Geology, 279, 55-

1017   62.

1018 Spear, F.S., and Kohn, M.J. (1996) Trace element zoning in garnet as a monitor of crustal

1019   melting. Geology, 24, 1099-1102.

1020 Spear, F.S., and Pyle, J.M. (2010) Theoretical modeling of monazite growth in a low-Ca

1021   metapelite. Chemical Geology, 273, 111-119.

1022 Spear, F.S., Kohn, M.J., and Cheney, J.T. (1999) P-T paths from anatectic pelites. Contributions

1023   to Mineralogy and Petrology, 134(1), 17-32.

1024 Spear, F.S., Thomas, J.B., and Hallett, B.W. (2014) Overstepping the garnet isograd: a

1025   comparison of QuiG barometry and thermodynamic modeling. Contributions to Mineralogy

1026   and Petrology, 168(1059).

1027 Spencer, K.J., Hacker, B.R., Kylander-Clark, A.R.C., Andersen, T.B., Cottle, J.M., Stearns,

1028   M.A., Poletti, J.E., and Seward, G.G.E. (2013) Campaign-style titanite U-Pb dating by laser-

1029   ablation ICP: Implications for crustal flow, phase transformations and titanite closure.

1030   Chemical Geology, 341, 84-101.

1031 Stübner, K., Grujic, D., Parrish, R.R., Roberts, N.M.W., Kronz, A., Wooden, J., and Ahmad, T.

1032   (2014) Monazite geochronology unravels the timing of crustal thickening in the NW

1033   Himalaya. Lithos, 210-211, 111-128.

1034 Terry, M.P., Robinson, P., Hamilton, M.A., and Jercinovic, M.J. (2000) Monazite geochronology

1035   of UHP and HP metamorphism, deformation, and exhumation, Nordøyane, Western Gneiss

1036   Region, Norway. American Mineralogist, 85, 1651-1664.

1037 Thöni, M., Miller, C., Hager, C., Grasemann, B., and Horschinegg, M. (2012) New

1038   geochronological constraints on the thermal and exhumation history of the Lesser and

38

1039   Higher Himalayan Crystalline Units in the Kullu-Kinnaur area of Himachal Pradesh (India).

1040   Journal of Asian Earth Sciences, 52, 98-116.

1041   Thompson, R. (1969) Àbátán: A master potter of the Ègbádò Yorùbá. In D. Biebuyck, Ed.

1042   Tradition and creativity in tribal art, p. 120-182. University of California Press, Berkeley.

1043   Tomkins, H.S., Powell, R., and Ellis, D.J. (2007) The pressure dependence of the zirconium-in-

1044   rutile thermometer. Journal of Metamorphic Geology, 25, 703-713.

1045   Vielzeuf, D., Veschambre, M., and Brunet, F. (2005) Oxygen isotope heterogeneities and

1046   diffusion profile in composite metamorphic-magmatic garnets from the Pyrenees. American

1047   Mineralogist, 90, 463-472.

1048   Vry, J.K., and Baker, J.A. (2006) LA-MC-ICPMS Pb-Pb dating of rutile from slowly cooled

1049   granulites: Confirmation of the high closure temperature for Pb diffusion in rutile.

1050   Geochimica et Cosmochimica Acta, 70, 1807-1820.

1051   Walther, J.V., and Wood, B.J. (1984) Rate and mechanism in prograde metamorphism.

1052   Contributions to Mineralogy and Petrology, 88, 246-259.

1053   Wang, J.M., Zhang, J.J., and Wang, X.X. (2013) Structural kinematics, metamorphic P-T

1054   profiles and zircon geochronology across the Greater Himalayan Crystalline Complex in

1055   south-central Tibet: implication for a revised channel flow. Journal of Metamorphic Geology,

1056   31, 607-628.

1057   Watson, E.B., and Harrison, T.M. (1983) Zircon saturation revisited; temperature and

1058   composition effects in a variety of crustal magma types. Earth and Planetary Science

1059   Letters, 64(2), 295-304.

1060   Watson, E.B., Wark, D.A., and Thomas, J.B. (2006) Crystallization thermometers for zircon and

1061   rutile. Contributions to Mineralogy and Petrology, 151, 413-433.

1062   Whitehouse, M.J., and Platt, J.P. (2003) Dating high-grade metamorphism – constraints from

1063   rare-earth elements in zircon and garnet. Contributions to Mineralogy and Petrology, 145,

1064   61-74.

1065   Yang, P., and Rivers, T. (2001) Chromium and manganese zoning in pelitic garnet and kyanite;

1066   spiral, overprint, and oscillatory (?) zoning patterns and the role of growth rate. Journal of

1067   Metamorphic Geology, 19(4), 455-474.

1068   Yang, P., and Rivers, T. (2002) The origin of Mn and Y annuli in garnet and the thermal

1069   dependence of P in garnet and Y in apatite in calc-pelite and pelite, Gagnon terrane,

1070   western Labrador. Geological Materials Research, 4,

1071   http://gmr.minsocam.org/contents.html.

1072   Ye, K., Liou, J.B., Cong, B.L., and Maruyama, S. (2001) Overpressures induced by coesite-

1073   quartz transition in zircon. American Mineralogist, 86(10), 1151-1155.

1074   Young, D.J., Hacker, B.R., Andersen, T.B., and Corfu, F. (2007) Prograde amphibolite facies to

1075   ultrahigh-pressure transition along Nordfjord, western Norway: Implications for exhumation

1076   tectonics. Tectonics, 26, doi:10.1029/2004TC001781.

1077   Young, D.J., Hacker, B.R., Andersen, T.B., and Gans, P.B. (2011) Structure and ^{40}Ar/^{39}Ar

1078   thermochronology of an ultrahigh-pressure transition in western Norway. Journal of the

1079   Geological Society, 168, 887-898.

1080   Zeng, L., Gao, L.-E., Dong, C., and Tang, S. (2012) High-pressure melting of metapelite and

1081   formation of Ca-rich granitic melts in the Namche Barwa Massif, southern Tibet. Gondwana

1082   Research, 21, 138-151.

1083   Zhang, Y.X. (1998) Mechanical and phase equilibria in inclusion-host systems. Earth and

1084   Planetary Science Letters, 157(3-4), 209-222.

1085

Figure Captions

1085

1086 Figure 1. Textural correlation of monazite ages with metamorphic petrogenesis in Himalayan

1087 rocks, central Nepal (from Catlos et al., 2001). (A) Similar ages of monazite inclusions near

1088 garnet rim and matrix monazite are interpreted to represent the timing of the peak of

1089 metamorphism. (B) Disparate ages from inclusion and matrix grains are interpreted to represent

1090 early prograde metamorphism and late stage recrystallization or resetting. Scale bars are all

1091 100 μm. Black circles are analytical locations.

1092 Figure 2. (A) Monazite inclusion chronology for single garnet from the Grouse Creek Mountains,

1093 NW Utah, showing a general decrease from core to rim (Hoisch et al., 2008). Inset shows

1094 schematically how monazites might be distributed through garnet; black monazite inclusions

1095 illustrate core vs. rim positions. Linear regression and 95% confidence limits (black lines) are for

1096 all data; green curve connecting young ages illustrates possible alternative growth history. Error

1097 bars are ±2σ. (B) All data from Hoisch et al. (2008) with possible alternative growth history

1098 connecting youngest inclusions.

1099 Figure 3. Mineral inclusions and ages in zircons from the Kaghan, Pakistan, UHP terrane. (A)

1100 Zircon domains with quartz inclusions average ~50 Ma whereas domains with coesite inclusions

1101 average ~47 Ma, but not all dated zircon domains contain inclusions. From Kaneko et al.

1102 (2003). Thin lines illustrate cathodoluminescent bands. (B) P-T conditions and path. Although

1103 the prograde P-T path (dashed line) is not directly constrained, in principle the entrapment

1104 conditions for quartz (blue hexagon) and coesite (magenta hexagon) could be similar, implying

1105 slow tectonic processes (heating at c. 3 °C/Ma), or disparate, implying rapid tectonic processes

1106 (heating at c. 50 °C/Ma). Large boxes indicate P-T conditions from different studies (see

1107 summary of Kohn, 2014).

1108 Figure 4. (A) Photomicrograph of garnet from Chile, showing dark clouds of fluid inclusions in

1109 garnet core and rim, and surrounding isolated mineral inclusions. These textures may reflect

1110 dissolution-reprecipitation (Putnis, 2002), which can penetrate into garnet along fracture

1111 channels and alter chemistry (and presumably age of inclusions) even after entrapment. Red

41

1112 box shows region of high-resolution images (Fig. 4D) (B-C) X-ray maps of garnet showing

1113 chemical reequilibration (low Ca, high Mn) in replaced zones. White box in Fig. 4C shows region

1114 of photomicrograph (Fig. 4A). (D) High-resolution images of isolated inclusions of quartz and

1115 plagioclase showing fluid inclusion clouds and chemical reequilibration of garnet without obvious

1116 physical connections to matrix.

1117 Figure 5. (A) Schematic of mineral with concentric chemical (temperature) zoning. The position

1118 of a composition, such as Mg#, is converted to closure temperature (T_c) and modeled in terms

1119 of cooling rate (s). (B) Schematic of mineral with concentric chronologic zoning. The position of

1120 an age (e.g., as represented by ^{206}Pb concentration for a fixed U content) is modeled in terms of

1121 closure temperature (T_c). Cooling rate (s) is determined from two T_c's and ages ($s=\Delta T_c/\Delta t$). (C)

1122 Uncertainties in retrieved cooling rate from chemical vs. chronologic zoning. Input cooling rate

1123 was 25 °C. Diffusion parameters are from Carlson (2006) for garnet. Uncertainties in activation

1124 energy (accounting for correlated changes to D_o) impose much larger errors in s using chemical

1125 rather than chronologic zoning.

1126 Figure 6. (A) Chemical zoning in garnet from Sikkim Himalaya, showing possible diffusion

1127 zoning in outer c. 100 μm. This zoning can be modeled with an average cooling rate of ~20

1128 °C/Ma. (B) Chemical zoning is present in all garnet components, suggesting that the edge

1129 position of the garnet has changed simultaneously with diffusion, complicating interpretation of

1130 temperature-time history. From Ganguly et al. (2000).

1131 Figure 7. (A) Chronologic depth profiles in rutile, collected via LA-ICP-MS, for rocks from the

1132 Ivrea Zone, southern Alps, showing decreasing ages towards rim. Inset illustrates how laser is

1133 used to ablate natural crystal face. Raw data from Smye and Stockli (2014; weighted averages

1134 and minimum uncertainties recalculated using equations 7 and 8a of Kohn and Spear, 1991a).

1135 Blue line drawn through averaged data is the same in both panels. (B) Cooling history

1136 calculated assuming diffusion parameters of Cherniak (2000) and inversion technique of

1137 Ketcham (2005). From Smye and Stockli (2014).

1138   Figure 8. P-T diagram illustrating schematically the chemical evolution of monazite in the

1139   context of garnet growth and partial melting. Prograde monazite grows up to the muscovite

1140   dehydration-melting reaction (stages 1 and 2), with decreasing Y and Th due to Y and Th

1141   scavenging during monazite and garnet growth. Monazite dissolves during melting (stage 3),

1142   and during melt crystallization (stage 4) retrograde monazite with high Y and Th grows on relict

1143   cores. Upper left inset shows X-ray maps of prograde chemical zoning in monazite from the

1144   southern Appalachians (Kohn and Malloy, 2004). Lower right inset shows X-ray maps of

1145   retrograde chemical zoning in monazite from anatectic rocks of the central Himalaya (Kohn et

1146   al., 2005).

1147   Figure 9. Age histograms of chemically-characterized monazite domains from the central

1148   Himalaya (Kohn et al., 2004, 2005; muscovite $^{40}Ar/^{39}Ar$ ages ("Ms" with arrow) from Herman et

1149   al., 2010). These data demonstrate steadily decreasing ages for any specific generation of

1150   monazite structurally downwards, consistent with in-sequence thrusting. (A) Simplified structural

1151   section and geologic map of Nepal showing the locations of Modi and Langtang transects and

1152   the main lithotectonic units (Greater Himalayan Sequence, GHS = orange, Lesser Himalayan

1153   Sequence, LHS = blue, Tethyan Himalayan Sequence = gray; leucogranites = red). The Main

1154   Central Thrust (MCT) separates the Greater and Lesser Himalayan Sequences. (B) Monazite

1155   ages expressed as probability densities and color coded according to interpretation of

1156   chemistry. (C) Composite temperature-time histories in the context of possible thermal evolution

1157   (dashed lines) for rocks from the Langtang transect. "Peak" = estimated age of peak

1158   metamorphism for LHS rocks from youngest prograde monazite ages. "Crystal" = age of

1159   crystallization of *in situ* melts from age of post-anatectic monazite rims. Thermobarometry

1160   constrains peak temperatures (Kohn, 2008). For each thrusting event, these data indicate

1161   simultaneous hanging-wall cooling during footwall heating.

1162   Figure 10. (A) Zircon and whole-rock REE patterns. NASC, MORB, and Pred. Zrn are the North

1163   American Shale Composite (Gromet et al., 1984), Mid-Ocean Ridge Basalt (Arevalo and

1164   McDonough, 2010) and zircon that would be in equilibrium with NASC assuming zircon–whole-

1165   rock partition coefficients of Sano et al. (2002). "Eu anom." = europium anomaly. "Detr. Core"

43

1166 and "Met. Rim" show measured detrital core and metamorphic rim for zircon from eclogite-facies

1167 rock, Italy (Rubatto, 2002). Inset shows sketch of zircon analyzed; thin lines represent

1168 oscillations evident from cathodoluminescence imaging. Scale bar is 50 μm. (B) REE patterns

1169 for garnet from the same eclogite-facies rock, showing evolution from steep to flat HREE pattern

1170 from core to rim (Rubatto, 2002). (C) Prediction of garnet stability field in metabasalt for two

1171 commonly used thermodynamic databases (Berman, 1988, modified in Berman and Aranovich,

1172 1996; Holland and Powell, 1998; see also Kohn et al., 2015), illustrating large field of garnet

1173 stability. Fields completely overlap in the area labeled "Berman".

1174 Figure 11. Temperature-time histories from combined U-Pb dating and Zr-thermometry of

1175 titanite. (A) Different domains from titanite in a single rock from the Greater Himalayan

1176 Sequence, Modi region, central Nepal. From Kohn and Corrie (2011). Insets show analytical

1177 methods (depth profiling vs. spot analyses) and domain-style compositional heterogeneity in

1178 backscattered electron image of titanite. Scale bar is 100 μm. (B) Titanite data from multiple

1179 rocks in the Western Gneiss Region UHP terrane, Norway (data from Spencer et al., 2013).

1180 Inset shows titanite stability field for typical Western Gneiss Region gneisses (Spencer et al.,

1181 2013). Modified from Kohn et al. (2015).

1182 Figure 12. (A) Schematic of expected Ti-in-Zrn and Zrn-saturation temperatures for migmatitic

1183 melts and leucogranites relative to T-t history of host rocks. Zircons should record temperatures

1184 at least as high as the host-rock temperature (Permissible Zone), not below the host-rock T-t

1185 curve (Forbidden Zone). Early formed lower-T zircons (e.g. c. 750 °C at 35 Ma) might not

1186 survive later heating (?'s in Permissible zone). The dry solidus corresponds to the temperature

1187 of the muscovite dehydration-melting reaction. The wet solidus accounts for possible low-P

1188 crystallization and presence of high B content. (B) Temperature-time points from combined

1189 zircon U-Pb dating and Ti-thermometry for Sikkim, India, region of the east-central Himalaya

1190 (data sources in Kohn, 2014). Ti-in-zircon thermometry suggests T ≤ ~700°C since 35 Ma and

1191 fall well below estimated peak metamorphic Ts, but are consistent with zircon-saturation

1192 thermometry of leucogranites and migmatitic segregations across the Himalaya (histogram;

1193 modified from Kohn, 2014, to include data from Scaillet et al., 1990; Guo and Wilson, 2012;

1194 Thöni et al., 2012; Zeng et al., 2012; Carosi et al., 2013; and Liu et al., 2014). A shift in

1195 monazite chemistry at 20–25 Ma (Rubatto et al., 2013) may indicate a transition to regional

1196 cooling. Proposed T-t curves are from Ganguly et al. (2000; G00; assuming peak age of 23 Ma),

1197 Harris et al. (2004; H04), Rubatto et al. (2013; R13), and Kellett et al. (2013; K13).

1198 Figure 13. (A-D) Zirconium mass balance models modified from Kohn et al. (2015) showing that

1199 zircon mode should decrease during prograde metamorphism, and increase during retrograde

1200 cooling. Points 1-5 reflect important mineralogical changes. (A, B) Mafic models. "+ Grt" =

1201 garnet stability fields predicted by the thermodynamic database of Holland Powell (1998) ("HP")

1202 vs. the thermodynamic database of Berman (1988) and Berman and Aranovich (1996) ("B").

1203 Rutile strongly controls amount of Zr available to zircon. (C-D) Pelitic model based on the

1204 Holland and Powell (1998) thermodynamic model. Melt strongly controls amount of Zr available

1205 to zircon. (E) Zircon ages from Western Gneiss Region superimposed on T-t path from titanite,

1206 showing that most ages are late-stage (post-UHP). Regional chronologic constraints from

1207 garnet (see summary of Kylander-Clark et al., 2009) and monazite (Terry et al., 2000) shown for

1208 reference. Modified from Kohn et al. (2015).

1209 Figure 14. (A) Calibration of the quartz-in-garnet (QuiG) and zircon-in-garnet (ZiG)

1210 thermobarometers (Kohn, 2014). Example of thermoba-Raman-try for rock from central

1211 Himalaya, Nepal (J Walters and M Kohn, unpubl. data) shows close correspondence with

1212 conventional thermobarometry (Corrie and Kohn, 2011). (B) Calibration of the quartz-in-titanite

1213 and quartz-in-zircon barometers (Kohn, 2014), illustrating good barometric potential (closely-
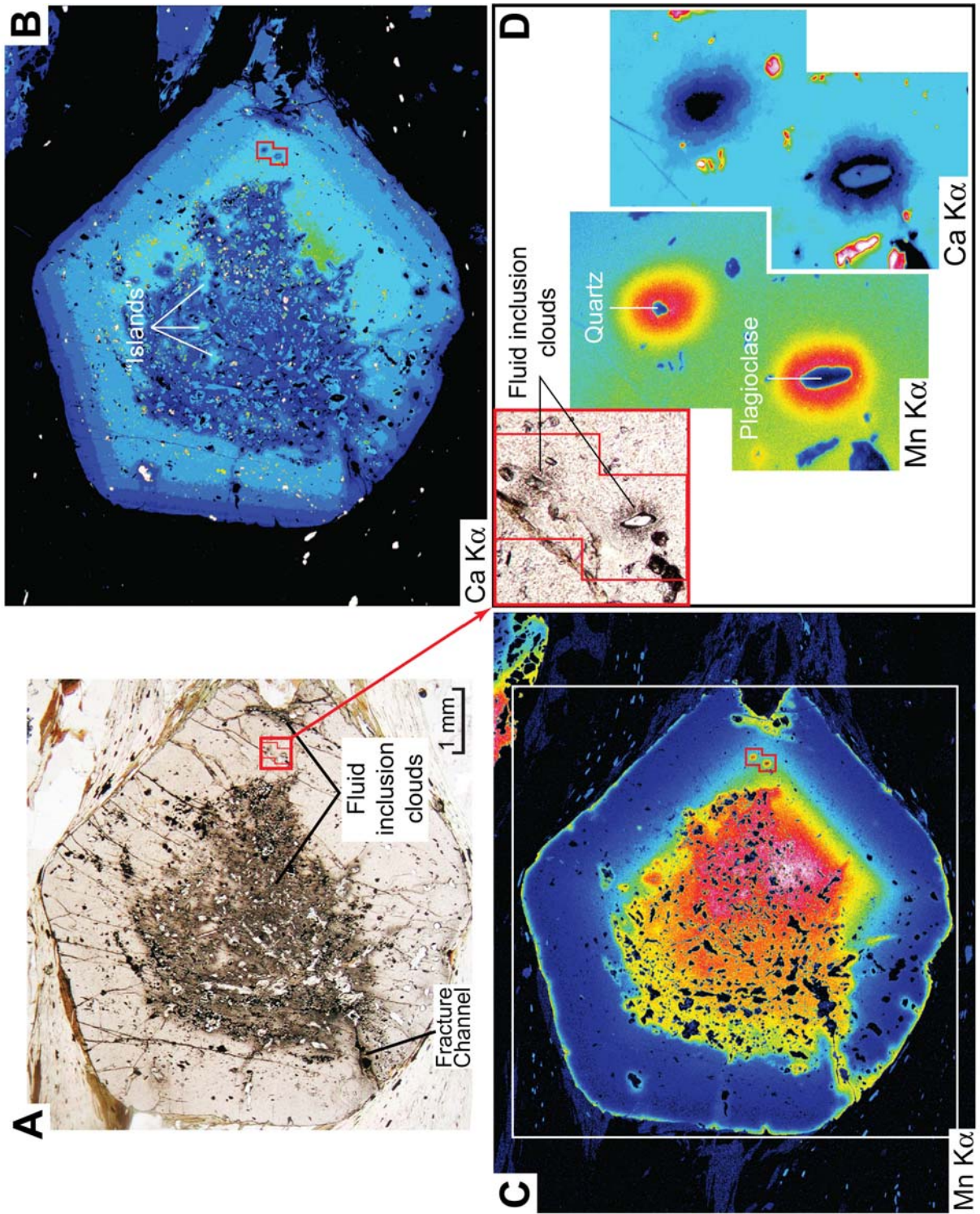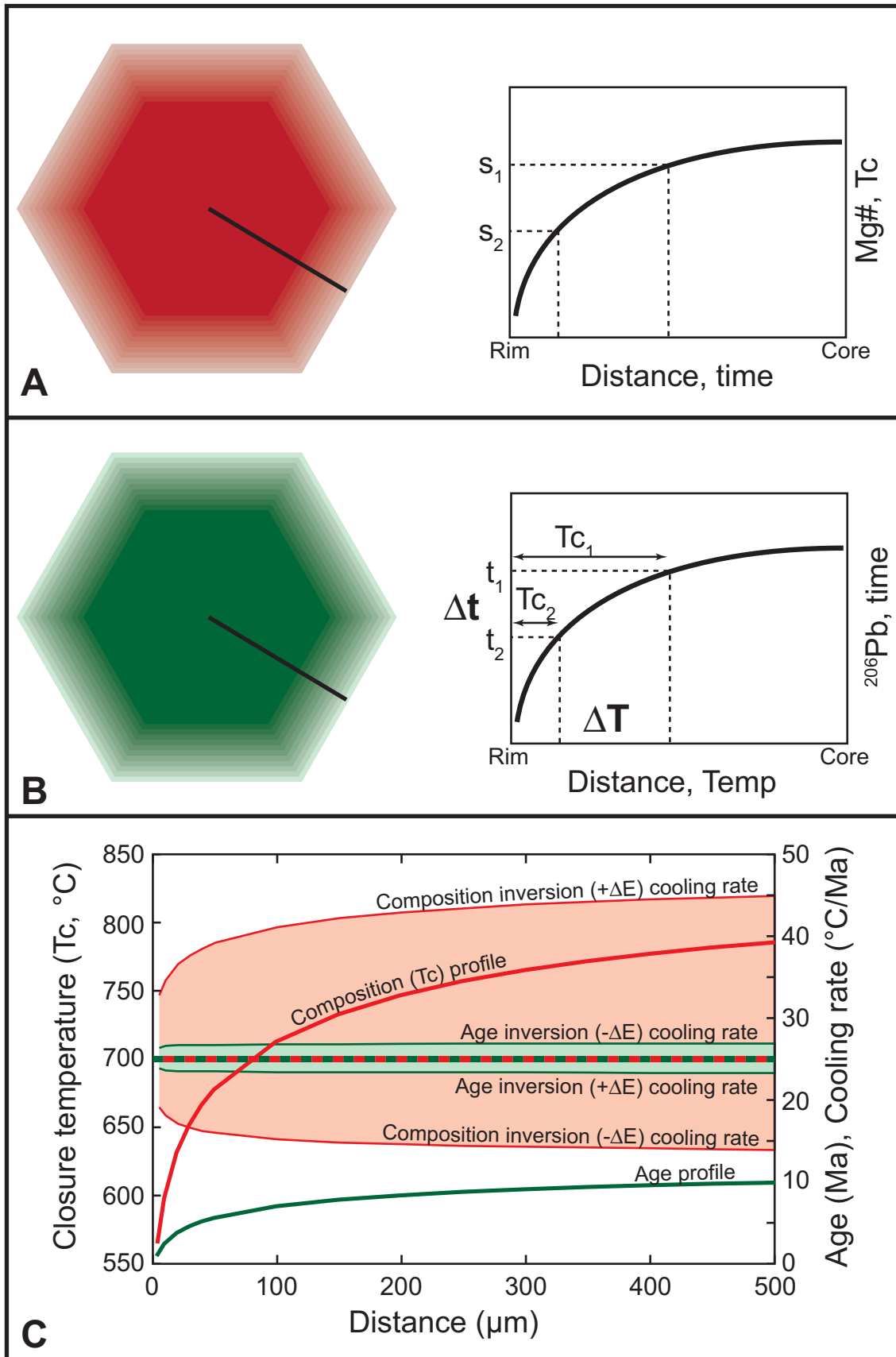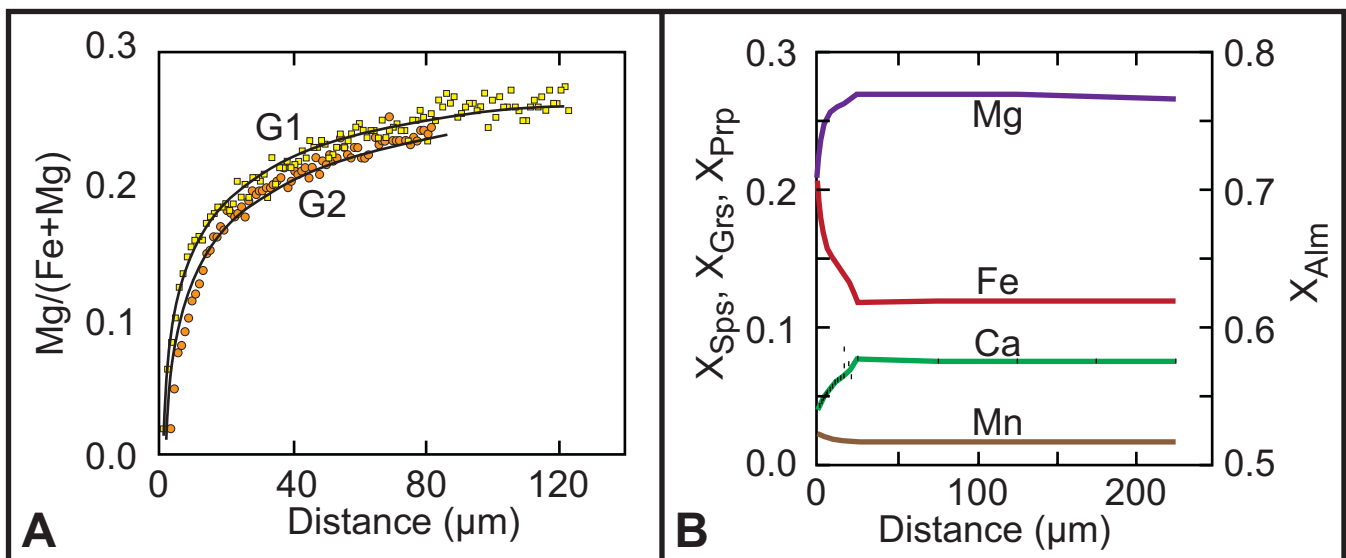
1214 spaced, flat isopleths).
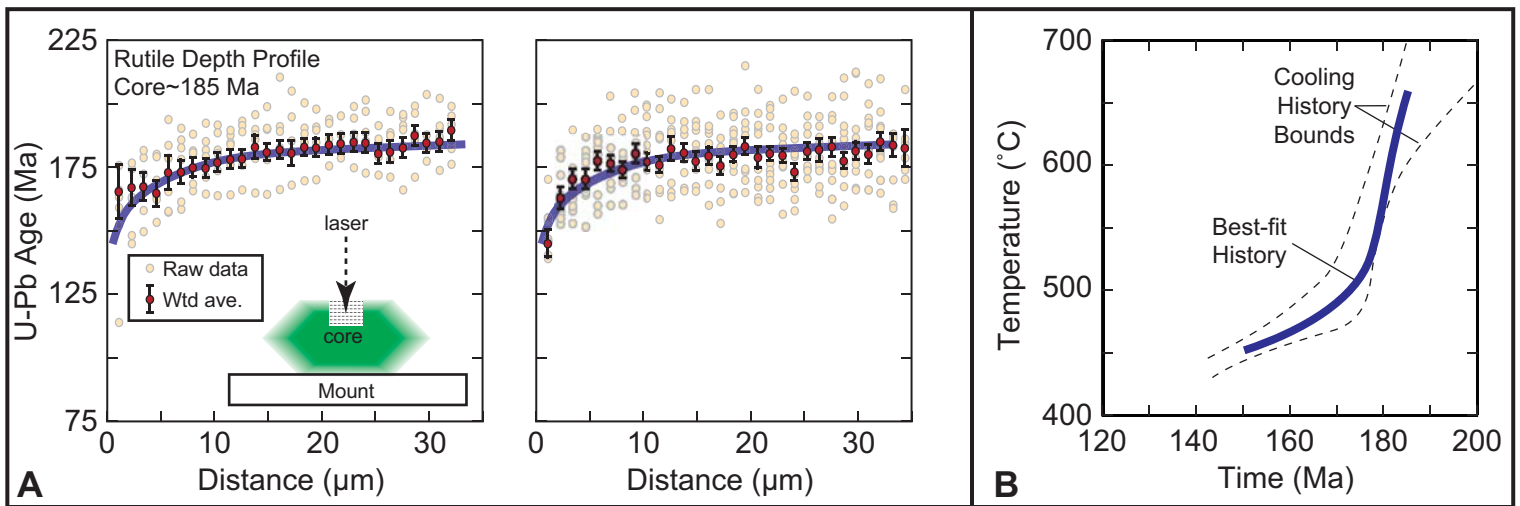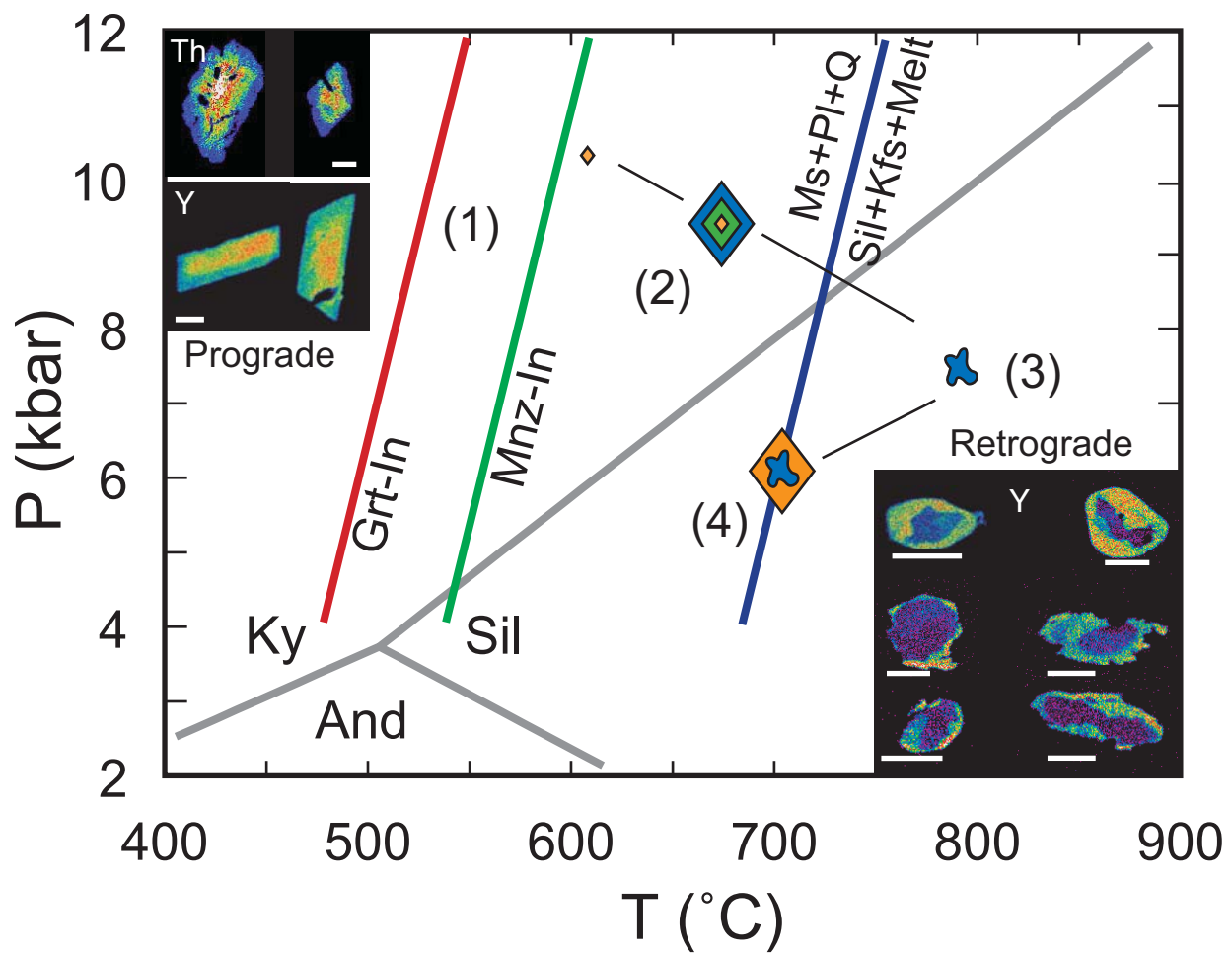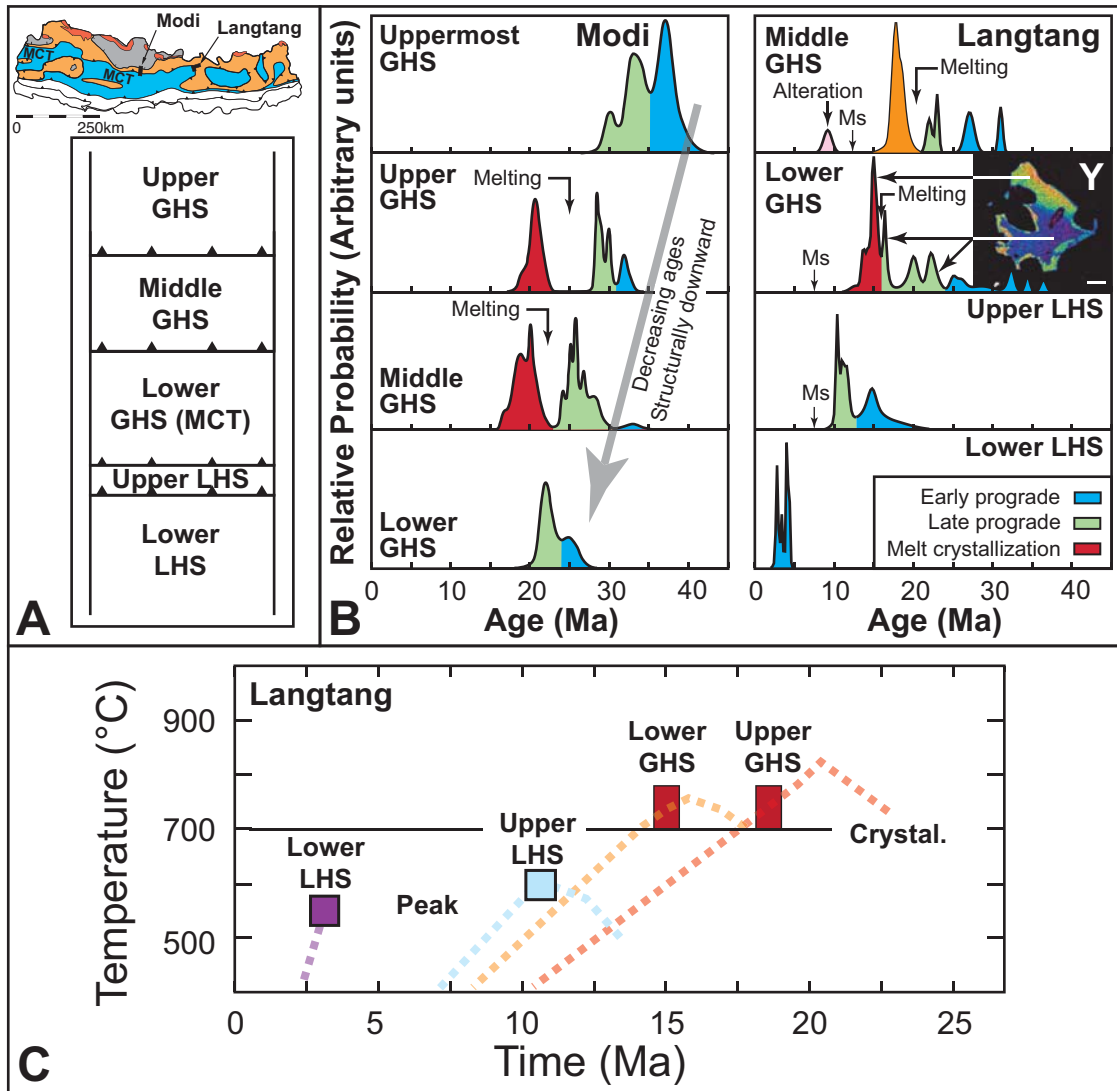
45
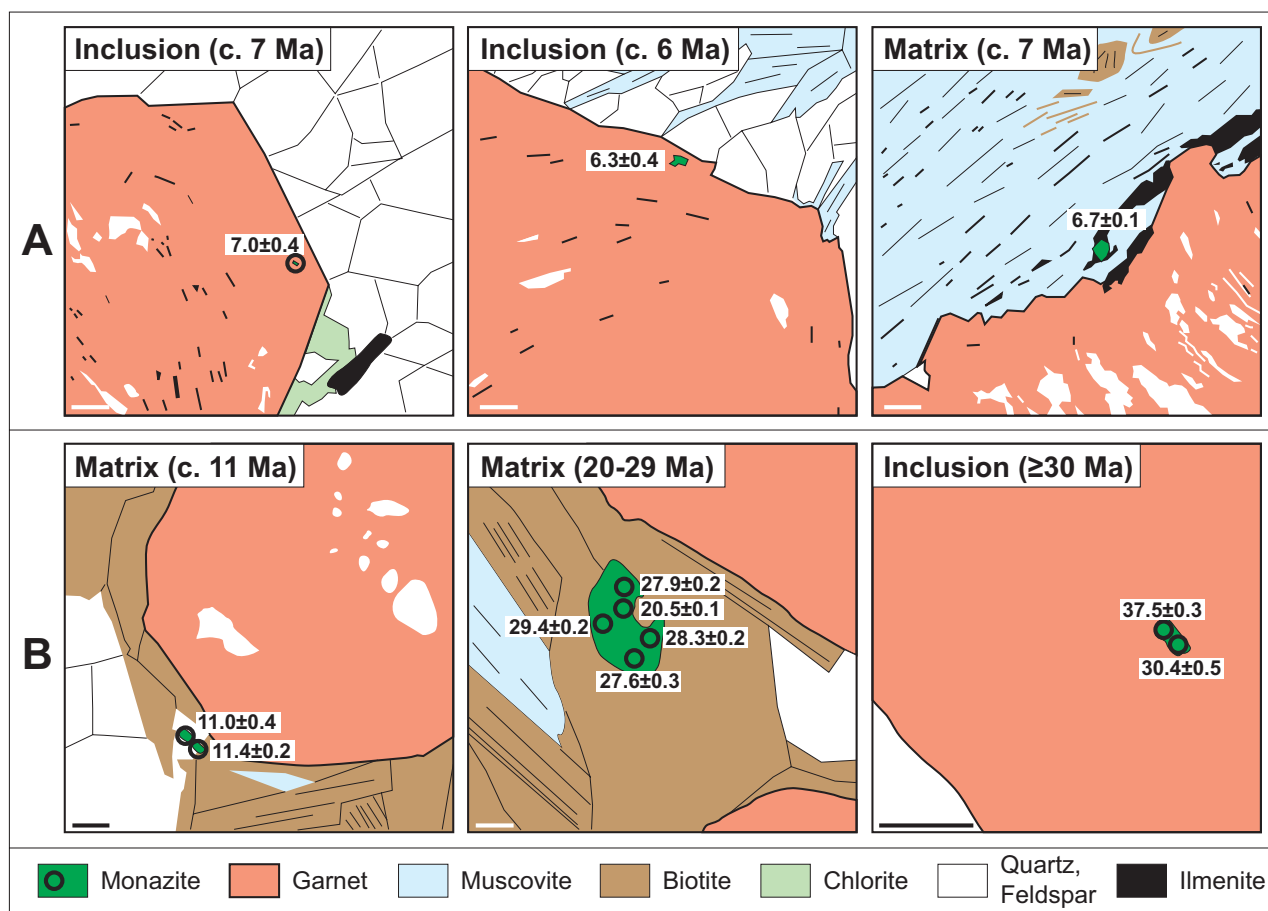
Kohn, Fig. 1
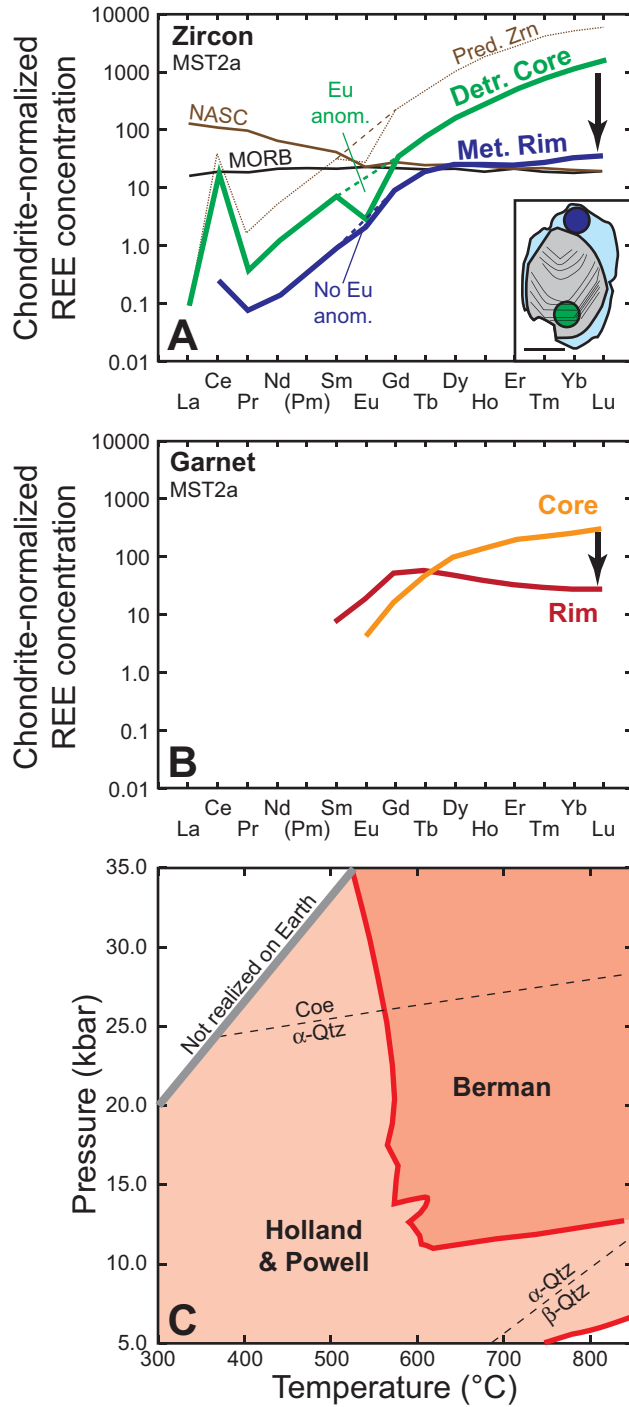
Kohn, Fig. 2
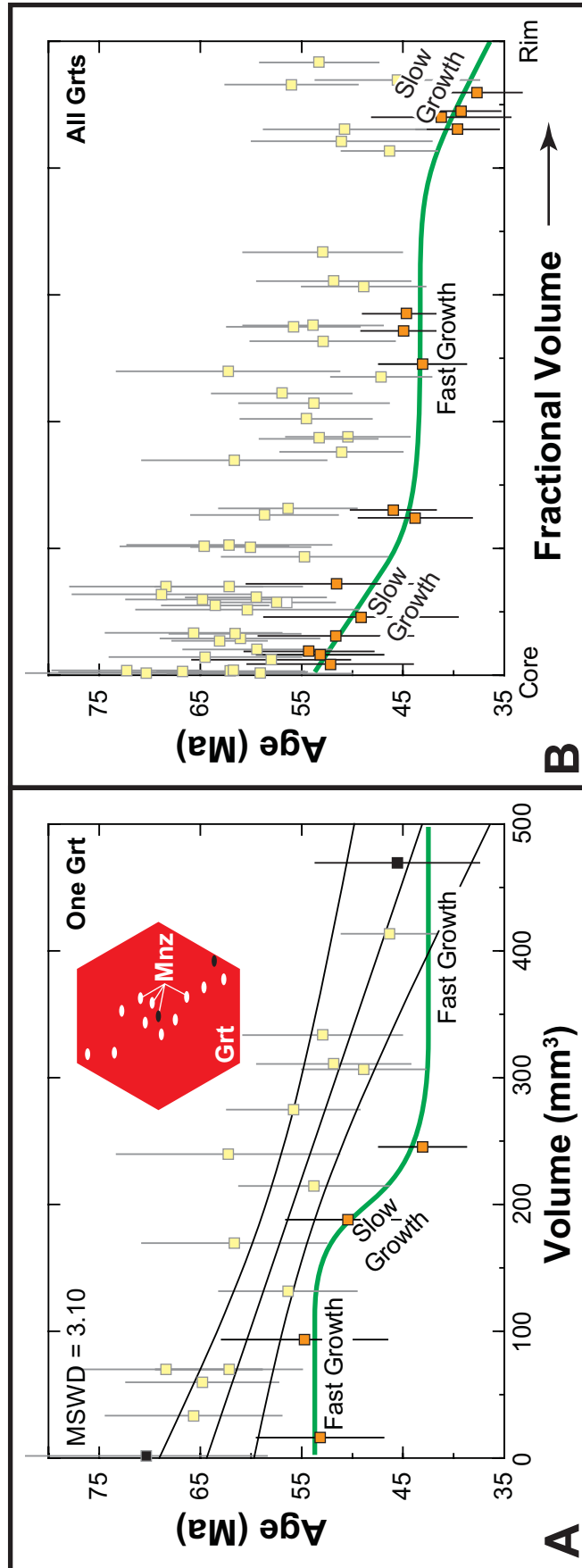
Kohn, Fig. 3
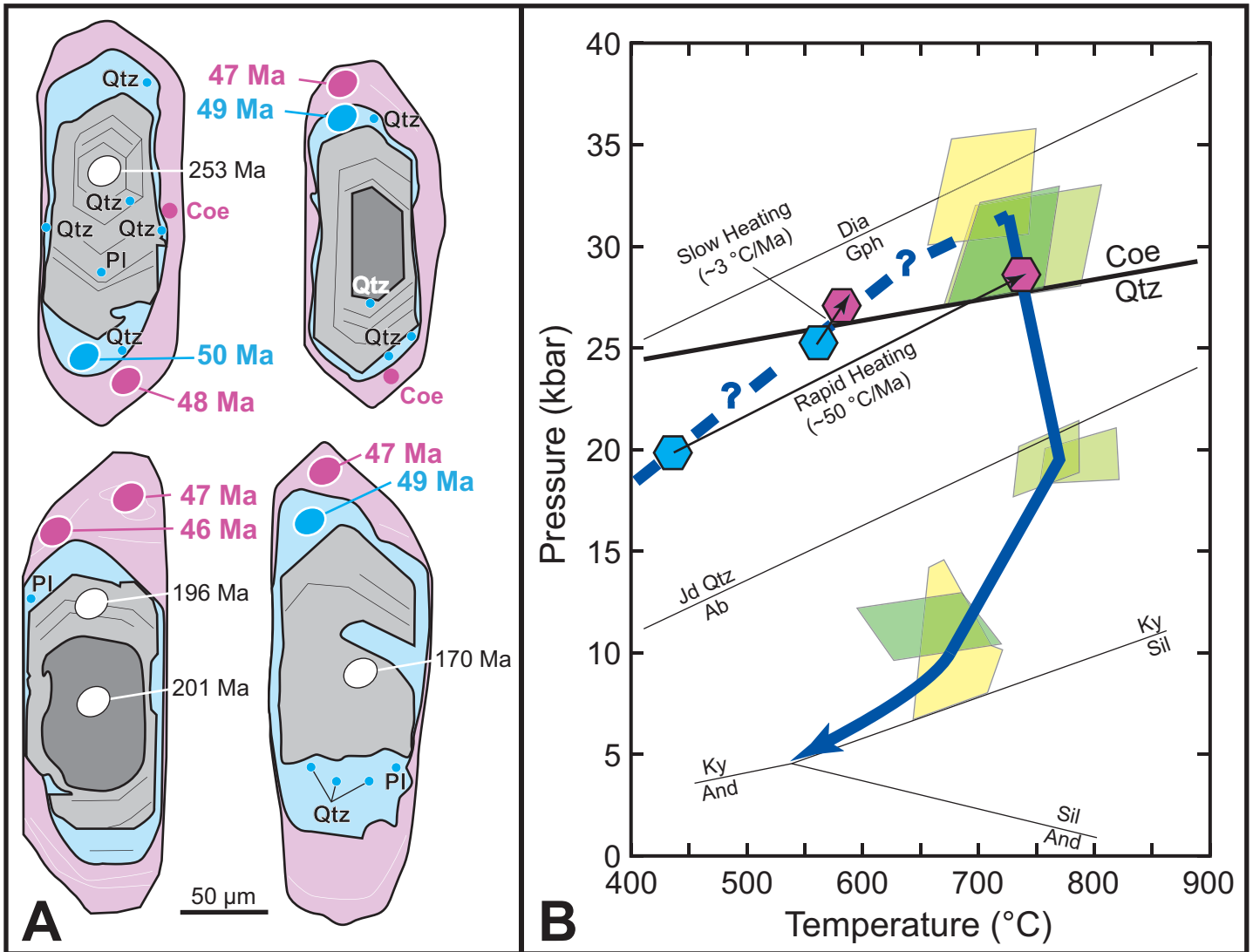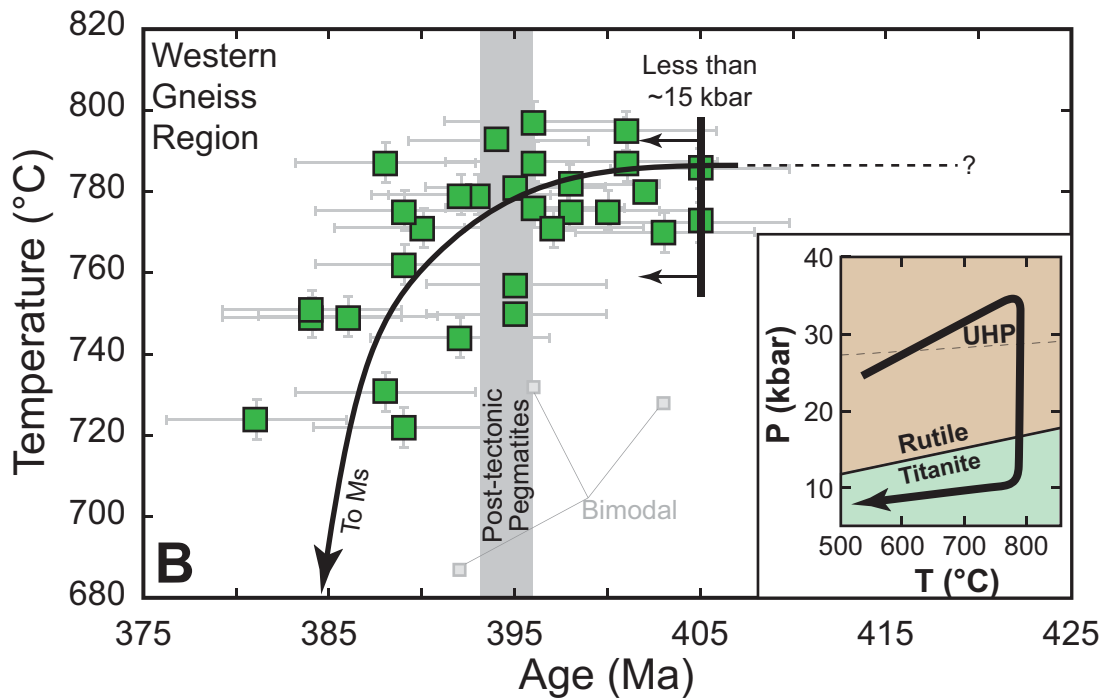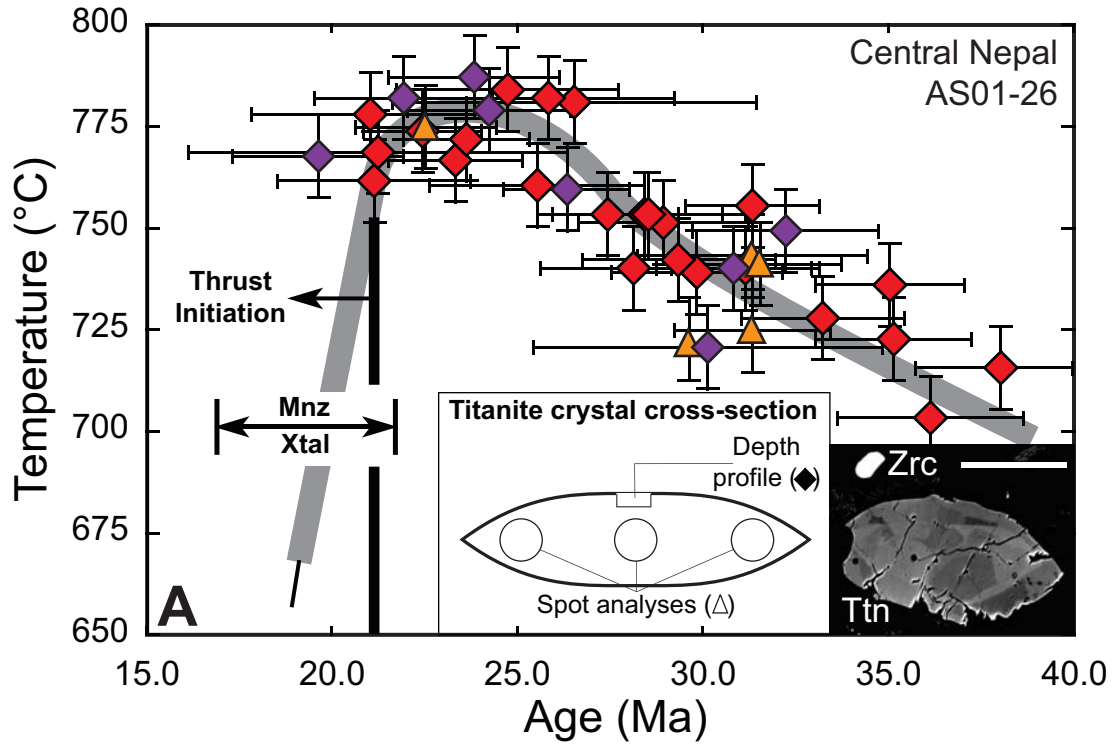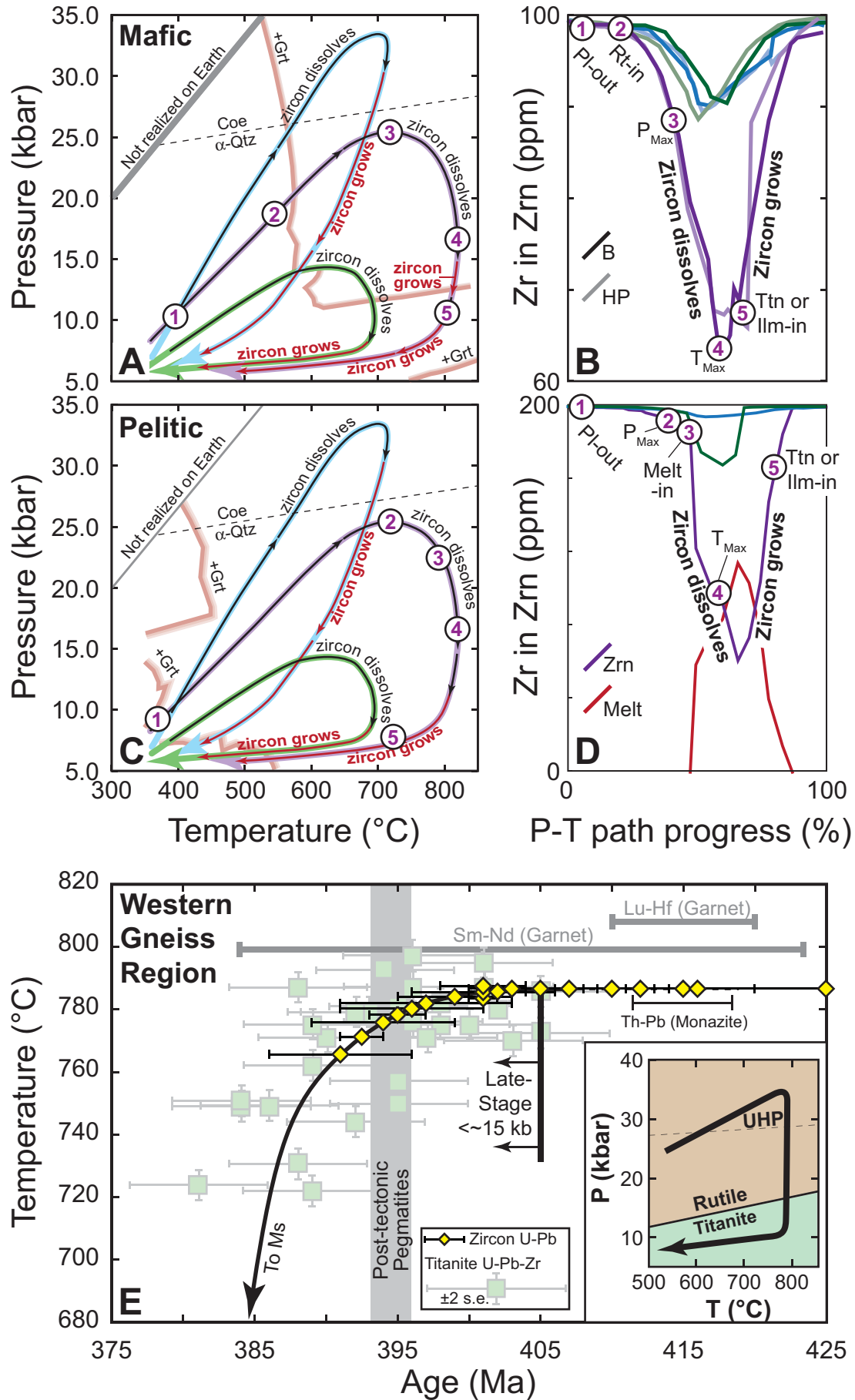
Kohn, Fig. 4

Kohn, Fig. 6

Kohn, Fig. 7

Kohn, Fig. 8

Kohn, Fig. 9

Kohn, Fig. 10

Kohn, Fig. 11

Kohn, Fig. 12

Kohn, Fig. 14